

Fractional Chern Insulator and Quantum Anomalous Hall Crystal in Twisted MoTe₂

Jialin Chen,^{1,*} Qiaoyi Li,^{1,2,*} Xiaoyu Wang,^{3,†} and Wei Li^{1,‡}

¹*Institute of Theoretical Physics, Chinese Academy of Sciences, Beijing 100190, China*

²*School of Physical Sciences, University of Chinese Academy of Sciences, Beijing 100049, China*

³*National High Magnetic Field Lab, Tallahassee, Florida 32310, USA*

Recent experimental advances have uncovered fractional Chern insulators in twisted MoTe₂ (tMoTe₂) systems, posing significant theoretical challenges in understanding the interaction effects and correlated topological phases. Here, we construct a realistic moiré lattice model tailored for tMoTe₂ and conduct investigations using state-of-the-art tensor-network methods. Our ground-state calculations reveal a rich array of interaction- and filling-dependent phases, including the FCI, Chern insulator, and generalized Wigner crystal, etc., explaining recent experimental observations. Moreover, we reveal quantum anomalous Hall crystals exhibiting integer Hall conductivity at fractional moiré unit cell fillings, which opens new avenues for experimental exploration in tMoTe₂. In the FCI phase, dynamical simulations reveal a single-particle continuum with a finite charge gap, indicating the presence of fractional charge excitations. Moreover, our finite-temperature calculations determine the characteristic temperatures for charge activation and ferromagnetic (FM) transitions, consistent with experiments. We find that the charge gap is significantly larger than the energy scales of both thermal activation and FM transitions, explaining recent experimental observations. Overall, by integrating ground-state, finite-temperature, and dynamical tensor-network calculations on the real-space model, we establish a theoretical framework for understanding and exploring correlated topological phases in tMoTe₂ and related systems.

I. INTRODUCTION

Twisted bilayer transition metal dichalcogenides, such as twisted MoTe₂ (tMoTe₂), have attracted great research interest for the intriguing topological and correlated quantum states [1–13]. The fractional Chern insulator (FCI) constitutes a hallmark of topological and strong correlation effects [1–5], and represents a long-sought phase in condensed matter physics. Following the detection of signatures through optical measurements [7, 8], recent transport experiments have successfully observed both the fractionally quantized Hall conductivity and the vanishing longitudinal conductivity [9, 10]. These findings provide direct evidence for the existence of FCI phase in tMoTe₂ at hole fillings $\nu_h = -2/3$ and $-3/5$. Subsequently, more FCI states are revealed at $\nu_h = -4/7$, $-4/9$, and $-5/9$ [11, 12], alongside a range of intriguing properties associated with these states. In particular, a defining feature of FCIs — the coexistence of conducting edge states and an insulating bulk — has been confirmed through local probes [13].

Understanding these novel topological states presents significant challenges for theoretical studies, as it requires addressing highly entangled many-body states. Accurate numerical calculations are indispensable for these investigations. Currently, the primary method employed is exact diagonalization (ED), which has been extensively used to study the continuum model of tMoTe₂ in momentum space [14–26]. However, these ED calculations mainly consider a single active band and are restricted to small clusters of about 30 sites, due to the (exponentially) high computational cost. Therefore, large-scale calculations are essential to study the corre-

lated topological states like FCI and enable comparisons with experiments.

On the other hand, the Hartree-Fock (HF) method has been utilized to explore the phase diagram of realistic models for tMoTe₂, by tuning parameters such as the displacement field [27–29], magnetic field [27], interaction strength [30, 31], and twist angle [26, 30, 31]. However, since Hartree-Fock variational wavefunctions are inherently product states, this method is fundamentally limited in its ability to capture highly entangled quantum phases, such as the FCI. Moreover, while the Hartree-Fock approximation systematically overestimates insulating gap sizes, and accurate many-body calculations are indispensable for reliably determining both charge and excitation gaps.

Furthermore, while experiments have explored a wide range of measurements [32] — including spectroscopy [8, 11, 13, 33], transport [9, 10], thermodynamics [7], magnetometry [12], and microstructural characterization [34] — most theoretical efforts have been devoted to ground-state studies. It thus leaves a critical gap in understanding dynamics and finite-temperature effects and interpreting the diverse experimental observations [35]. For instance, a key challenge arises from the significant discrepancy between thermodynamic gaps measured in local magnetometry experiments (14 ± 1 meV at $\nu_h = -1$ and 7.0 ± 0.5 meV at $\nu_h = -2/3$) and charge activation gaps obtained from transport measurements (32 ± 2 K and 23 ± 7 K for the respective fillings) [9, 12]. This nearly five-fold difference in energy scales demands theoretical clarification to advance our understanding of the related topological quantum states.

To address these critical questions and bridge the gap in understanding tMoTe₂, we conduct a comprehensive tensor-network study based on a realistic, Hubbard-type model in real space (see Fig. 1). Starting from a microscopic continuum electronic model, we derive tight-binding parameters by constructing appropriate Wannier orbitals, enabling us to formulate a Hamiltonian with realistic hopping parameters. We em-

* These authors contributed equally to this work.

† xywangmn@gmail.com

‡ w.li@itp.ac.cn

ploy the density matrix renormalization group (DMRG) [36–38] for zero-temperature calculations, the tangent-space tensor renormalization group (tanTRG) [39, 40] for thermodynamics, and the time-dependent variational principle (TDVP) [41, 42] to study dynamical properties. Our unbiased large-scale tensor-network calculations enable a comprehensive and experimentally relevant investigation of tMoTe₂, offering a unified framework to interpret diverse experimental observations and generating novel predictions to guide future studies.

Our ground-state studies reveal the experimental discovered FCI states for various electron fillings $1/3 \leq \nu < 1$, or hole fillings $-1 < \nu_h \leq -1/3$ via particle-hole transformation (as explained below), alongside a competition between CO and FCI states (see Fig. 1e). We further reveal the existence of quantum anomalous Hall crystal (QAHC) states — characterized by the coexistence of integer Hall conductivity and CO at fractional fillings such as $\nu = 1/2$ and $2/3$ — which have not yet been observed in tMoTe₂. We further propose that these QAHC states could be transitioned into FCI states by melting their charge order through tuning parameters like dielectric constant and temperature.

Our finite-temperature calculations identify FM phase transitions at T_c , which exhibits a non-monotonic behavior versus fillings, in agreement with experimental observations [8]. Furthermore, we also compute the single-particle spectral function at zero temperature, for several representative fillings including $\nu = 1/2, 2/3$, and 1 , and identify the charge gaps as approximately 18.2 meV, 8.4 meV, and 6.2 meV, respectively. Dynamical simulations further yield results of the local density of state at the Fermi level $A_{\text{loc}}(\omega = 0)$, which disclose a typical thermal activation temperature of about $T^* \approx 30$ K for $\nu = 1/3, 2/3, 1$, in agreement with recent experiments (with the same filling) of longitudinal resistance measurements [9]. Notably, the zero-temperature charge gaps are found to be significantly larger than the energy scales of thermal activation and FM transition, a phenomenon that has been observed in experiments but lacks theoretical basis [10, 12]. Our numerical results reproduce these experimental observations and resolve their contradictions with the realistic real-space model, which establish a robust foundation for further theoretical and experimental investigations on MoTe₂ and moiré materials in general.

II. MODEL AND METHODS

A. Real-Space Model on the Honeycomb Lattice

Bilayer MoTe₂ with a twist angle of approximately 3.89° has recently attracted significant experimental interest [7–12]. To provide a theoretical understanding, density functional theory (DFT) calculations [6, 18, 19, 43, 44] have been conducted to reveal the relevant low-energy degrees of freedom. They comprise two bands per valley with Chern numbers +1 and -1, respectively. Due to the spin-valley locking [45], the spin- \uparrow state is associated with valley **K**, while the spin- \downarrow state is linked to valley **K'**, resulting in a minimal model encompassing four electronic bands. For simplicity, we refer primarily

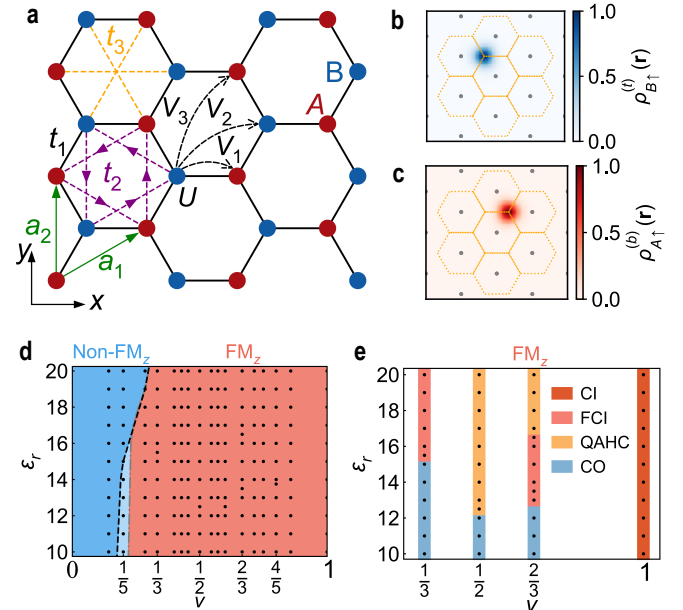


FIG. 1. Real-space model on the honeycomb lattice and its global phase diagram. **a** Schematic representation of the model with hopping parameters (t_1, t_2, t_3) and interactions (U, V_1, V_2, V_3) up to the third nearest neighbor on a honeycomb lattice. $\alpha_1 = (\sqrt{3}/2, 1/2)$ and $\alpha_2 = (0, 1)$ denote the primitive vectors of the honeycomb lattice. Numerical simulations employ a X-cylinder (XC) geometry with periodic boundary conditions along α_2 direction. Panels **b** and **c** show real-space electronic density profile of exponentially localized Wannier orbitals, normalized to the peak density. $\rho_{i\uparrow}^{(l)} = |w_{i\uparrow}^{(l)}|^2$ for spin- \uparrow is centered on site $i = (A, B)$ in layer $l = (b, t)$. The Wannier orbitals reside mostly at the honeycomb lattice sites, corresponding to the XM/MX stacking regions of the twisted bilayer MoTe₂. **d** Magnetic phase diagram in the ϵ_r - ν plane, where the dashed line (obtained with $N_y = 5$ cylinder) and dash-dotted boundary lines ($N_y = 4$ data) separate the FM_z and non-FM_z phases. **e** Phase diagrams with representative fillings ($\nu = 1, 2/3, 1/2$, and $1/3$) contains various phases, including the CI, FCI, QAHC, and CO phases.

to the spin states throughout the manuscript, omitting explicit reference to the valley degree of freedom. It has been shown that the low energy physics of tMoTe₂ can be effectively described by a continuum model [6] (see also SM I [46]), which can be mapped to a tight-binding model through a proper choice of Wannier basis, through the trial state procedure [23, 30, 47]. As illustrated in Fig. 1b and c, the Wannier orbitals $w_{i\uparrow}^{(l)}$ for spin- \uparrow are exponentially localized on the two sublattices ($i = A$ or B) of a honeycomb lattice [47] and exhibit clear layer resolution ($l = b$ or t , meaning bottom or top). Specifically, $w_{A\uparrow}^{(b)}$ predominantly resides on the bottom layer, while $w_{B\uparrow}^{(t)}$ resides on the top layer. The situation is the same for spin- \downarrow orbitals since the two spin orientations are related by the time-reversal symmetry.

By projecting the kinetic term and Coulomb interactions onto these Wannier orbitals, we derive a Hubbard-type real-space model for tMoTe₂ on the honeycomb lattice, as depicted

in Fig. 1a. The Hamiltonian reads

$$H = \sum_{(i,j)} (t_{ij} c_{i\uparrow}^\dagger c_{j\uparrow} + t_{ij}^* c_{i\downarrow}^\dagger c_{j,\downarrow} + h.c.) - \mu \sum_i n_i + U \sum_i n_{i\uparrow} n_{i\downarrow} + \sum_{i < j} V_{ij} n_i n_j, \quad (1)$$

where $c_{i\sigma}^\dagger$ ($c_{i\sigma}$) creates (annihilates) an electron with spin $\sigma = \uparrow, \downarrow$ on site i . The density at site i is $n_i = n_{i\uparrow} + n_{i\downarrow}$, with $n_{i\sigma} = c_{i\sigma}^\dagger c_{i\sigma}$. μ is the chemical potential, and the hopping parameter t_{ij} is between the (i, j) pair for electrons with spin- \uparrow , conjugate to those for spin- \downarrow . We consider the hopping amplitudes (t_1, t_2, t_3) , up to the third nearest neighbor in our model (see Fig. 1a). Notably, the next-nearest neighbor hopping t_2 for spin- \uparrow electrons along the direction depicted in Fig. 1a incorporates a phase factor of $\phi = 2\pi/3$. Therefore, hopping parameters (for spin- \uparrow) are $t_1 = -3.225$ meV, $t_2 = 2.120e^{i2\pi/3}$ meV, and $t_3 = 0.947$ meV.

The onsite Coulomb interaction is denoted as $U = 1192.71/\epsilon_r$ meV, where ϵ_r represents the relative dielectric constant (see SM I [46]). For the further couplings V_{ij} , we consider a dual-gate screened Coulomb interaction in tMoTe₂, i.e.,

$$V(r) = \frac{e^2}{4\pi r \epsilon_0 \epsilon_r} e^{-r/\xi} = \frac{276.92}{\epsilon_r r/L_m} \exp\left(-\frac{r/L_m}{\xi/L_m}\right) \text{ meV},$$

where ϵ_0 is the vacuum permittivity, r is the distance between two sites, and ξ is the screening length. $L_m \simeq 5.2$ nm represents the length of primitive vectors of the moiré lattice (see Fig. 1a), which is taken as the unit of length in the present study. In our simulations, we mainly consider $10 \leq \epsilon_r \leq 20$ in tMoTe₂, aligning with previous studies [18, 23, 27]. Additionally, we adopt a reasonable value of $\xi/L_m = 2$, as also used in Ref. [23], and retain interaction terms up to the third nearest neighbor [i.e., V_1, V_2, V_3 as indicated in Fig. 1a], compatible with our finite width of cylinder (up to 6). Such a truncation in V_{ij} (and also t_{ij}) turns out to be a good approximation, even for large $\xi = 30$ nm $\simeq 5.77 L_m$, as illustrated in SM I [46].

Since the onsite Coulomb interaction U exceeds the hopping parameters t_1, t_2, t_3 by over an order of magnitude, we can project out double occupancy at low temperatures. The numerical benchmarks between two models are shown in the SM III [46]. Then we arrive at a spinful t - V model whose Hamiltonian reads

$$H = \sum_{i < j} (t_{ij} P_i c_{i\uparrow}^\dagger c_{j\uparrow} P_j + t_{ij}^* P_i c_{i\downarrow}^\dagger c_{j,\downarrow} P_j + h.c.) - \mu \sum_i n_i P_i + \sum_{i < j} V_{ij} P_i n_i n_j P_j, \quad (2)$$

where $P_i = 1 - n_{i\uparrow} n_{i\downarrow}$ is a projector on site i . The spin-spin coupling J can be neglected as $U \gg |t_{ij}|$ and thus $|t_{ij}|^2/U \ll 1$ [23]. This projected spinful t - V model is utilized in our finite-temperature (and also part of ground-state) calculations.

In the calculations of fully spin-polarized cases, e.g., FCI and QAHC states, we further simplify the model to a spinless version. This is justified as Eq. [2] conserves electron

numbers for both spin flavors, and the spinless Hamiltonian is given by

$$H = \sum_{i < j} (t_{ij} c_i^\dagger c_j + h.c.) - \mu \sum_i n_i + \sum_{i < j} V_{ij} n_i n_j, \quad (3)$$

where c_i^\dagger creates an electron at site i , and $n_i = c_i^\dagger c_i$ is the particle number operator. This spinless t - V model is employed in the calculation of Hall conductivity, and its validity is confirmed by comparing the results with those from the Hubbard-type model [1] or the spinful t - V model [2]. The three models and their usage in various simulations are summarized in Table I.

Here for the sake of simplicity, we have performed a particle-hole transformation in the model [1]. It inverts the hopping parameters and chemical potential, thus the non-interacting band structure [19] (see also SM I [46]). In the following, we use ν to denote the electron filling per unit cell, which consists of two lattice sites, A and B . Consequently, the experimentally relevant hole filling $-1 \leq \nu_h \leq 0$ thus corresponds to the electron filling $0 \leq \nu \leq 1$ in our practical model calculations. Moreover, to reduce computational costs, the Hubbard-type model described by Eq. [1] can be simplified to either a spinful or spinless t - V model (see Materials and Methods).

B. Tensor Network Methods

In this study, we investigate the zero-temperature, finite-temperature, and dynamical properties using state-of-the-art tensor-network methods (see Methods) on an X-cylindrical (XC) geometry of size $N_y \times N_x \times 2$.

For the ground state, we utilize both finite and infinite density matrix renormalization group (DMRG and iDMRG) [36–38, 48]. The iDMRG method is based on the infinite matrix product states (MPS) constructed from an enlarged unit cell with size $N_y \times N_x^c \times 2$. This approach allows us to explore the periodicity of the state by varying the size of unit cell, with the consistency of results confirmed through comparison to finite DMRG results. In practice, we retain a bond dimension up to $\chi = 4,096$ in iDMRG simulations, and the truncation errors $\lesssim 2 \times 10^{-5}$, thereby guaranteeing very good convergence and thus high accuracy of the results. In finite-size DMRG calculations, we fine-tune the total particle number to maintain bulk filling at $\nu \simeq p/q$ for integer p and q .

After obtaining the ground state, we employ real-time evolution with the TDVP approach [41, 42] to compute the retarded Green's function and subsequently derive the single-

Model	No.	d	$T = 0$	$T > 0$	Dynamics
Hubbard-type	Eq. [1]	4	✓	✓	✗
spinful t - V	Eq. [2]	3	✓	✓	✗
spinless t - V	Eq. [3]	2	✓	✗	✓

TABLE I. Real-space models used in tensor-network calculations. Here d refers to the dimension of local Hilbert space.

particle spectral function via Fourier transformation. In the computation of dynamical properties, it is necessary to determine the chemical potential μ beforehand in order to fix the position of the Fermi level ($\omega = 0$). In the present study, we estimate μ based on low-temperature calculations (practically at $T \simeq 1.45\text{K}$), utilizing the μ - ν relation (see, e.g., Fig. 6f). In practice, a Parzen window is applied to suppress non-physical oscillations [49, 50], achieving an energy resolution of 2.67 meV (with evolution time up to 3 meV^{-1}). We choose time step $\delta t = 1/16\text{ meV}^{-1}$ and bond dimension $\chi = 1000$, which renders accurate results in the TDVP calculations. The data convergence and more technical details are presented in the SM IV [46].

The tanTRG method [39] is employed to study the finite-temperature properties of the system. An accurate matrix product operator representation of the density matrix, with bond dimension χ up to 2000, enables us to investigate systems with sizes up to $\text{XC4} \times 24 \times 2$ and down to a low temperature of $T \simeq 1.45\text{ K}$ (i.e., $T/t_1 \simeq 0.0375$). In our tanTRG calculations, we employ the grand canonical ensemble and implement a specially designed chemical potential μ -tuning technique to precisely control the particle number. To study the FM transition, we introduce a small pinning field $h = 0.01$ to stabilize the FM order in the finite-size systems. To improve the efficiency, we implement Abelian spin and/or charge symmetries in the simulations and adopt controlled bond expansion techniques [51, 52] to speed up the finite-temperature calculations.

III. GROUND-STATE RESULTS

A. Global phase diagram

Since the presence of FM order has been experimentally identified as a prerequisite for the emergence of FCI and other exotic topological states in MoTe_2 [7–13], we first examine the emergence of FM order, characterized by full polarization of spin- S_z (denoted as FM_z). To evaluate the ground-state magnetism across various filling factors, we compare the energies of different S_z sectors in our iDMRG simulations (see SM II [46]). Our results reveal a finite energy gap above the FM_z ground state for $\nu \gtrsim 0.2$, as indicated by darker blue shading in Fig. 1d for $N_y = 4$ and 5. Additionally, for $N_y = 6$, we find that FM_z order remains robust at filling factors $\nu = 1, 2/3, 1/2$, and $1/3$, consistent with recent experimental observations [7, 8].

To investigate the presence of quantized Hall conductivity in the FM_z phases, we employ a charge pumping method [53–55] within our iDMRG simulations. As depicted in the inset of Fig. 2g, for filling factors $\nu = p/q$, we adiabatically introduce a flux of $\Phi_y = 2q\pi$ along the cylinder axis by modulating the hopping terms with a phase factor $e^{i\Phi_y} c_{i\sigma}^\dagger c_{j\sigma} + h.c.$ as the electron traverses the periodic boundary. For a charge pumping of ΔQ , the corresponding Hall conductivity is given by $\sigma_{xy} = \frac{2\pi|\Delta Q|}{\Phi_y}$, whose unit is set as e^2/h in this study.

Our simulations, primarily conducted for fillings $\nu = p/q$

and $q = 1, 2, 3$, reveal the existence of quantized Hall conductivity σ_{xy} , as indicated in Fig. 1e. We also consider $q = 5, 7, 9$ cases on $N_y = 4, 5$ cylinders, with the results summarized in SI Appendix Fig. S8 [46]. Notably, we successfully observe experimentally relevant $\sigma_{xy} = \nu = 1$ for CI states [46] and $\sigma_{xy} = \nu = 2/3, 4/7, 5/9, 4/9, 3/5$ for FCIs. Intriguingly, we predict a robust FCI state with $\sigma_{xy} = \nu = 1/3$ and advocate for its experimental observation in future studies. Moreover, we also identify instances where an integer Hall conductivity of $\sigma_{xy} = 1$ can be observed at fractional fillings $\nu = 1/2, 2/3$ (for $N_y = 6$ cylinder), as well as at $\nu = 3/5$ and $4/5$ (for $N_y = 5$). These integer Hall states coexist with COs that are compatible with the cylinder geometry, leading to the formation of QAHC states.

Regarding the COs, we have thoroughly examined the charge density distribution $n(\mathbf{r})$ in real space and $\rho(\mathbf{q}) = \frac{1}{\sqrt{N}} |\sum_i e^{i\mathbf{q}\cdot\mathbf{r}_i} (\langle n_i \rangle - \bar{n})|$ in momentum space, where \mathbf{r}_i labels the position of a unit cell (rather than the individual A/B site), revealing the existence of CO states. As illustrated in Fig. 1e (highlighted in blue), these topologically trivial CO states are located in the lower-left corner of the phase diagram, characterized by low fillings and strong interactions. Below we firstly show the DMRG results for different ν fillings, and then present our dynamical and finite-temperature simulation results.

B. Identification of FCI for $\nu = 1/3$

To start, we consider the filling fraction $\nu = 1/3$, and present the results on $N_y = 5$ and 6 cylinders. Our results reveal that the ground states exhibit FM_z order for a broad range of ϵ_r values, specifically $10 \leq \epsilon_r \leq 23$. For the regime with a relatively small ϵ_r , a GWC phase appear in the phase diagram Fig. 2a. The real-space charge density $n(\mathbf{r})$ is centered at the A sublattice and forms a triangular lattice with primitive vectors $\mathbf{a}_1^t = (\sqrt{3}, 0)$ and $\mathbf{a}_2^t = (\sqrt{3}/2, 3/2)$, thus breaking the translational symmetry of the original honeycomb lattice (see Fig. 2d). Correspondingly, in Fig. 2e we find clear peaks in $\rho(\mathbf{q})$ at the vertices (\mathbf{K} points), namely, the characteristic reciprocal vectors $\mathbf{b}_1^t = (0, 4\pi/3)$ and $\mathbf{b}_2^t = (-2\sqrt{3}\pi/3, 2\pi/3)$ of the triangular lattice. The results confirm the presence of a triangular GWC for relatively small ϵ_r .

However, for a larger relative dielectric constant, e.g., $\epsilon_r = 18$, the charge density $n(\mathbf{r})$ becomes uniformly distributed across the honeycomb lattice (Fig. 2f). As a result, $\rho(\mathbf{q})$ becomes negligible across the entire momentum space (Fig. 2a). As seen in Fig. 2a, the maximum of $\rho(\mathbf{q})$ undergoes a sharp drop to very small values at $\epsilon_r^c = 15.5$. For even larger $\epsilon_r > 23$, the ground state no longer has an FM_z order.

To characterize the transitions between GWC and FCI, we compute the charge-charge correlations $g^{nn}(\mathbf{r}) = \frac{\langle n_0 n_j \rangle}{\langle n_0 \rangle \langle n_j \rangle}$ between the charge density n_0 at a fixed site and other charge densities n_i located at site i . This metric provides insights into the attractive ($g^{nn} > 1$) and repulsive ($g^{nn} < 1$) correlations between electrons. As depicted in Fig. 2b for $\epsilon_r = 18$, we find $g^{nn} < 1$ for the first three nearest neighbors of the reference site, indicating a repulsive interaction among elec-

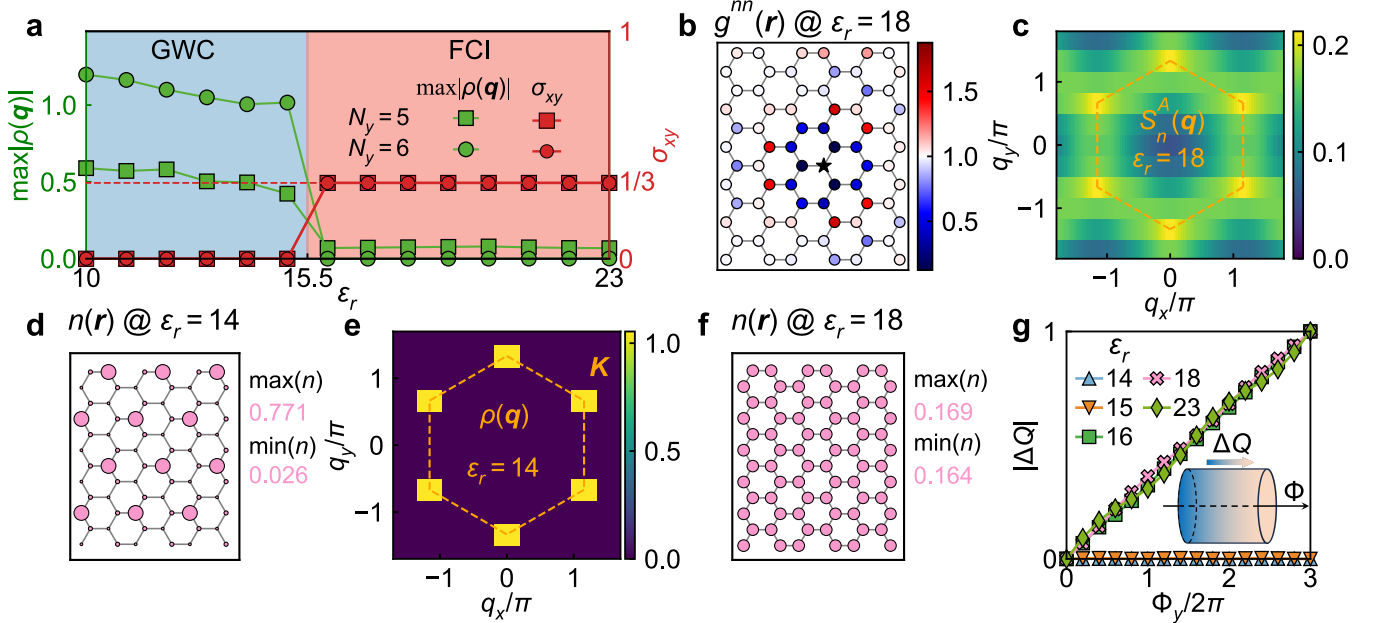


FIG. 2. GWC and FCI phases for $\nu = 1/3$ filling. **a** Phase diagram containing the GWC and FCI states tuned by the relative dielectric constant ϵ_r . The two phases are characterized by $\rho(\mathbf{q})$ and the Hall conductivity σ_{xy} , obtained on $N_y = 5$ and 6 cylinders. **b** Charge-charge correlation function $g^{nn}(\mathbf{r})$ in the FCI phase (with $\epsilon_r = 18$), displaying the charge distribution relative to the reference site n_0 marked by a black star. **c** Charge structure factor $S_n^A(\mathbf{q})$ in momentum space of the FCI state. Charge distribution **d** $n(\mathbf{r})$ in real-space and **e** $\rho(\mathbf{q})$ in momentum space for the GWC state (with $\epsilon_r = 14$), showcasing the triangular lattice pattern of electron density modulation. **f** demonstrates $n(\mathbf{r})$ for the FCI state ($\epsilon_r = 18$), where a uniform charge distribution is observed. **g** Charge pumping results $|\Delta Q|$ for various ϵ_r for $N_y = 6$, measured after inserting a flux $\Phi_y = 6\pi$. The inset illustrates the charge pumping simulation process. For this and subsequent plots, the dashed hexagon (c.f., panels **c** and **e**) outlines the first Brillouin zones of the honeycomb lattice.

trons within this close proximity. However, g^{nn} exceeds 1.0 for the fourth and fifth nearest neighbors, suggesting an attractive correlation in this region. This oscillating pattern of repulsion and attraction can extend even further away from the reference site, which constitutes a characteristic of neutral collective excitation, roton, in a FCI liquid [56].

We examine the charge structure factor $S_n^A(\mathbf{q})$ on the A sublattice

$$S_n^A(\mathbf{q}) = \frac{1}{N} \left| \sum_{i,j \in A} e^{i\mathbf{q}(\mathbf{r}_i - \mathbf{r}_j)} (\langle n_i n_j \rangle - \langle n_i \rangle \langle n_j \rangle) \right|, \quad (4)$$

which quantifies the spatial distribution of charge correlations in momentum space. In Fig. 2c, we plot $S_n^A(\mathbf{q})$ for $\epsilon_r = 18$ in the uniform state with $\rho^m(\mathbf{q}) \simeq 0$. The $S_n^A(\mathbf{q})$ peaks at the K points, which reflect the oscillating pattern observed in $g^{nn}(\mathbf{r})$. The positions of the peaks align with those of the GWC peaks depicted in Fig. 2e, indicating that the condensation of roton modes may be responsible for the transition from a uniform FCI to a triangular-lattice GWC.

Moreover, we simulate the Hall conductivity through charge pumping, as illustrated in Fig. 2g for several values of ϵ_r and $N_y = 6$, using iDMRG calculations. Our results demonstrate that inserting a flux of $\Phi_y = 6\pi$ induces a charge pumping of $|\Delta Q| = 1$ (thus $\sigma_{xy} = 1/3$) for FCIs, while $|\Delta Q| = 0$ for GWCs. By combining the Hall conductivity σ_{xy} and the charge distribution results, we construct the phase diagram in Fig. 2a: For $10 \leq \epsilon_r \leq 15.5$, the system resides in

a topologically trivial GWC phase with $\sigma_{xy} = 0$; in contrast, within the range $15.5 < \epsilon_r \leq 23$, the ground state transitions to a uniform FCI state with a quantized Hall conductivity of $\sigma_{xy} = 1/3$.

C. Emergence of QAHC for $\nu = 2/3$

Figure 3 presents our findings at fractional filling $\nu = 2/3$. Systematically scanning the parameter space reveals a robust FM_{*z*} ordered ground state for $\leq \epsilon_r$ between 10 and at least 30 across $N_y = 4, 5, 6$ cylinders. In Fig. 3a, we present the results of $\rho(\mathbf{q})$ and charge pumping for various ϵ_r and widths. Notably, for a system width of $N_y = 6$, the system transitions from a CO state at relatively small $\epsilon_r < 13$, to a uniform FCI state with maximum of $\rho(\mathbf{q}) \simeq 0$ and $\sigma_{xy} = 2/3$ for $13 \leq \epsilon_r \leq 16.5$. Furthermore, for $\epsilon_r > 16.5$ (and up to about $\epsilon_r \approx 30$), a QAHC state emerges with Hall conductivity of $\sigma_{xy} = 1$ and an underlying GWC order.

We emphasize that the QAHC state exhibits strong geometric sensitivity. For the $N_y = 6$ cylinder, we observed a quantized Hall conductivity of $\sigma_{xy} = 1$; however, such a state is absent for $N_y = 4$ and $N_y = 5$. This can be understood by examining the underlying charge distributions. In Fig. 3b, we show real-space charge distribution $n(\mathbf{r})$, where the maximum density $n \simeq 0.470$ and minimum density close to zero. In Fig. 3c, the holes form a triangular GWC structure with a

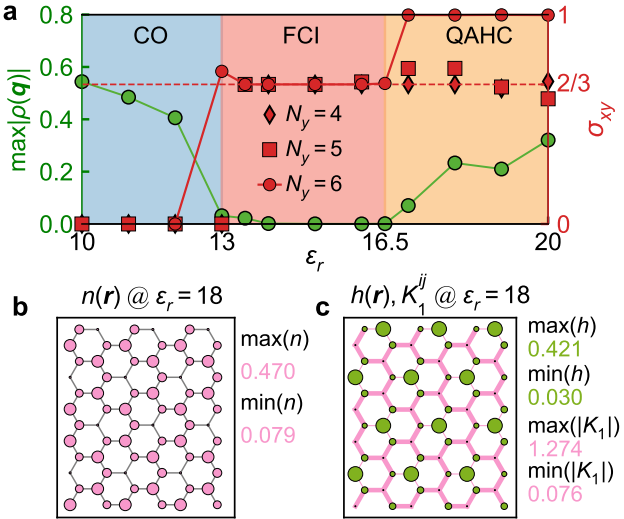


FIG. 3. Emergence of QAHC states for $\nu = 2/3$ filling. **a** Phase diagram containing CO, FCI, and QAHC phases versus ϵ_r , characterized by $\rho(\mathbf{q})$ and σ_{xy} . **b** Charge density $n(\mathbf{r})$ and **c** hole density $h(\mathbf{r})$, K_1^{ij} distributions in the QAHC state obtained with $\epsilon_r = 18$ and on $N_y = 6$ cylinder. As we define an average density of $n = 0.5$ (per site) as the “full” filling $\nu = 1$ (per unit cell) of the CI phase, the hole filling is thus $h(\mathbf{r}) = 0.5 - n(\mathbf{r})$, as depicted by green dots. The pink lines in panel **c** show the absolute values of K_1^{ij} (see definition in the main text).

period of 3 along the width (**a**₂) direction, which is compatible with the width $N_y = 6$.

Furthermore, in Fig. 3c we show the absolute values of nearest hopping $K_1^{ij} = \left| \left\langle t_1 \sum_{\sigma} (c_{i\sigma}^{\dagger} c_{j\sigma} + h.c.) \right\rangle \right|$, represented by the pink lines. Notably, the hopping between the largest green hole dots and other sites is virtually absent, suggesting that these holes are “immobile” and isolated from the electron background. Consequently, the QAHC can be interpreted as a composite state comprising an CI state of electrons with $\nu = 1$ (thus Hall conductivity $\sigma_{xy} = 1$) and a GWC of holes with density $\nu_h = -1/3$. Such an QAHC is also named hole crystal state [35]. Moreover, as shown in Fig. 3a for $N_y = 4$ and 5, the FCI state (with possible COs coexisting) exists, instead of QAHCs, due to the lattice geometry mismatches and has $\sigma_{xy} = 2/3$.

D. Even-odd effects for $\nu = 1/2$

Besides the fractional fillings $\nu = p/q$ with odd denominators q discussed above, we also consider an even- q filling fraction $\nu = 1/2$ in this study. As shown in Fig. 4b, charge pumping simulations on systems with an odd width $N_y = 5$ (with $\epsilon_r = 12$) find a fractional Hall conductivity $\sigma_{xy} = 1/2$, indicating the emergence of a FCI state. However, the same simulations on even-width systems with $N_y = 4, 6$ (with a different $\epsilon_r = 18$, though) find an integer Hall conductivity $\sigma_{xy} = 1$, indicating the presence of QAHC state.

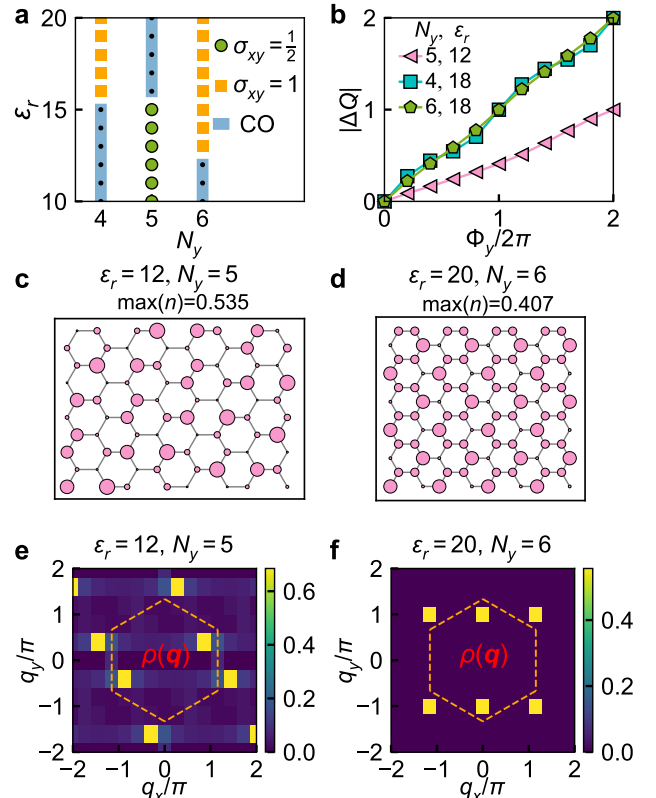


FIG. 4. FCI and QAHC for $\nu = 1/2$ filling. **a** The quantized σ_{xy} results obtained from charge pumping for various ϵ_r and N_y . **b** Charge pumping $|\Delta Q|$ after inserting flux $\Phi_y = 4\pi$, for FCI and QAHC states with different ϵ_r and N_y . Panels **c,e** show $n(\mathbf{r})$ and $\rho(\mathbf{q})$, respectively, revealing non-uniform charge distribution for the FCI state obtained with $N_y = 5$ and $\epsilon_r = 12$. Panels **d,f** show results of the QAHC state for $N_y = 6$ and $\epsilon_r = 20$.

To understand such even-odd effect, we compare the COs in the ground states. In Fig. 4, we show that for $N_y = 5$, the charge distribution $n(\mathbf{r})$ is incommensurate with the honeycomb lattice and $\rho(\mathbf{q})$ shows peaks at $(0.866\pi, 0.4\pi)$ and $(-0.866\pi, -0.4\pi)$. In contrast, for $N_y = 6$, a well defined commensurate CO emerges, as evidenced by the $(0, \pm\pi)$ peaks of $\rho(\mathbf{q})$ in momentum space. The emergence of a commensurate CO in even N_y systems, and its absence for odd N_y , may explain the odd-even effect for $\nu = 1/2$ filling. For even N_y , the CO with an enlarged unit cell allows an integer filling of the folded band (see Fig. 5c and related discussions below), yielding integer Hall conductivity. This offers an alternative explanation for the presence of QAHC, different from the hole crystal picture discussed above for $\nu = 2/3$. Note that the two scenarios, namely hole crystal and band folding for QAHC, are not strictly independent or mutually exclusive. Note that recent ED calculations at select k -points have also reported a QAHC state at $\nu = 1/2$ filling [24]. Here our large-scale simulation results further reveal a sensitive even-odd width dependence in the ground state.

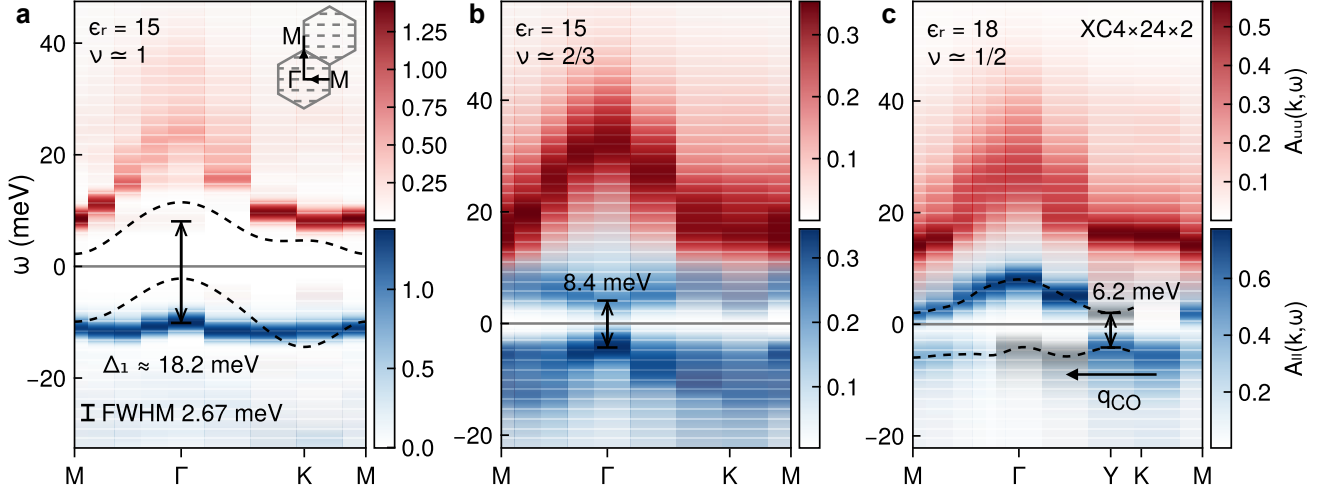


FIG. 5. Charge excitation spectra in CI, FCI and QAHC phases. The band-resolved spectral functions $A_{uu}(\mathbf{k}, \omega)$ and $A_{ll}(\mathbf{k}, \omega)$ simulated at zero temperature are shown for **a** CI state at $\nu = 1$, **b** FCI state at $\nu = 2/3$, and **c** the QAHC state at $\nu = 1/2$. The followed path in the reciprocal space is indicated in the inset of **a**. As a comparison, the bare band dispersion (without interactions) is illustrated by the dashed lines in **a**. The gray shadow in **c** represents the band folding with vector $\mathbf{q}_{CO} = (0, -\pi)$. The peaks of the two folded bands are marked by dashed lines (serving as a guide for the eye). The frequency resolution is approximately 2.67 meV, as indicated by the range bar in **a**.

IV. EXCITATION GAP AND CHARGE CONTINUUM

To study the dynamical properties, we compute the band-resolved spectral functions $A_{mm}(\mathbf{k}, \omega) \equiv -2\text{Im}G_{mm}^R(\mathbf{k}, \omega)$ of the CI state at $\nu = 1$, the FCI state at $\nu = 2/3$, and the QAHC state at $\nu = 1/2$. $G_{mm}^R(\mathbf{k}, \omega)$ is the retarded Green's function and $m = u, l$ labels the upper/lower band (see SM III [46] for details). The dynamical results reveal distinct features for these topological states, including the flattened band, charge excitation continuum, and band folding, providing valuable insights into their distinct nature.

Starting from the $\nu = 1$ CI phase in Fig. 5a, we find the lower band becomes significantly flattened compared to the bare band (with interactions turned off), highlighting the correlation effect. Additionally, a band gap of approximately $\Delta_1 \approx 18.2$ meV is obtained, with the Fermi level lying within the gap, consistent with the gapped CI phase at $\nu = 1$. On the other hand, in Fig. 5b, regarding the FCI state with $\nu = 2/3$, both the upper and lower bands exhibit significant broadening. The charge excitation continuum, instead of well-defined quasi-particle modes, signposts the emergence of fractional charge excitations in the FCI phase. Moreover, between the two broad “sub-bands”, there exists a charge gap $\Delta_{2/3} \approx 8.4$ meV, where the Fermi level resides, supporting a gapped nature of FCI. The charge gaps at $\nu = 1$ and $\nu = 2/3$ align well with the experimental results of 14 ± 1 meV and 7.0 ± 0.5 meV, respectively, as obtained by direct magnetic imaging at a low temperature of 1.6 K [12].

Lastly, for the QAHC phase at $\nu = 1/2$, as shown in Fig. 5c, the lower band also splits into two sub-bands, with a charge gap $\Delta_{1/2} \approx 6.2$ meV. Unlike the charge-uniform FCI states, there exists shadow bands near, e.g., the Γ point in the lower sub-band. This characteristic feature suggests the

occurrence of Brillouin zone folding, due to the presence of CO in the QAHC phase. Considering the CO wave vector $\mathbf{q}_{CO} = (0, \pm\pi)$, as observed from $\rho(\mathbf{q})$ in Fig. 4f, we shift the spectra of the lower two sub-bands. As seen in Fig. 5(c), the spectral weights shift from the $Y-M$ segment to $\Gamma-Y$, resulting in two folded bands. The Fermi level lies within the gap between these two bands, with the lower folded band being significantly flatter than the bare band. This closely resembles the band structure of the $\nu = 1$ CI state shown in Fig. 5a. Thus, our dynamical calculations further support that the QAHC state at $\nu = 1/2$ represents a Chern insulator coexisting with charge order in an enlarged unit cell.

V. CHARACTERISTIC TEMPERATURE SCALES

In Fig. 6, we present various finite-temperature properties calculated using the state-of-the-art finite-temperature tensor network method, tanTRG [39]. As shown in Fig. 6c, the specific heat curves $c_e = \frac{1}{N} \left(\frac{\partial E}{\partial T} \right)_\nu$ exhibit prominent peaks at certain critical temperatures T_c , for fillings $\nu = 1, 1/2, 2/3$, indicating the occurrence of FM transitions. To identify the FM transitions, we compute the averaged magnetic moment $m^z = \frac{1}{2} \frac{\sum_i \langle n_{i\uparrow} - n_{i\downarrow} \rangle}{\sum_i \langle n_{i\uparrow} + n_{i\downarrow} \rangle}$, and show the results in Fig. 6d. As temperature decreases, the magnetic moment m^z increases rapidly near T_c and converges to a polarized value of 0.5 for $T < T_c$, evidencing a FM transition. In addition to the cases with $\nu = 1, 1/2, 2/3$, we also present results for the $\nu = 1/3$ case in Fig. 6. Here, m^z displays an increasing trend (though it has yet to converge to saturation), suggesting that the FM transition occurs below the lowest temperature of 1.45 K attained in the simulations.

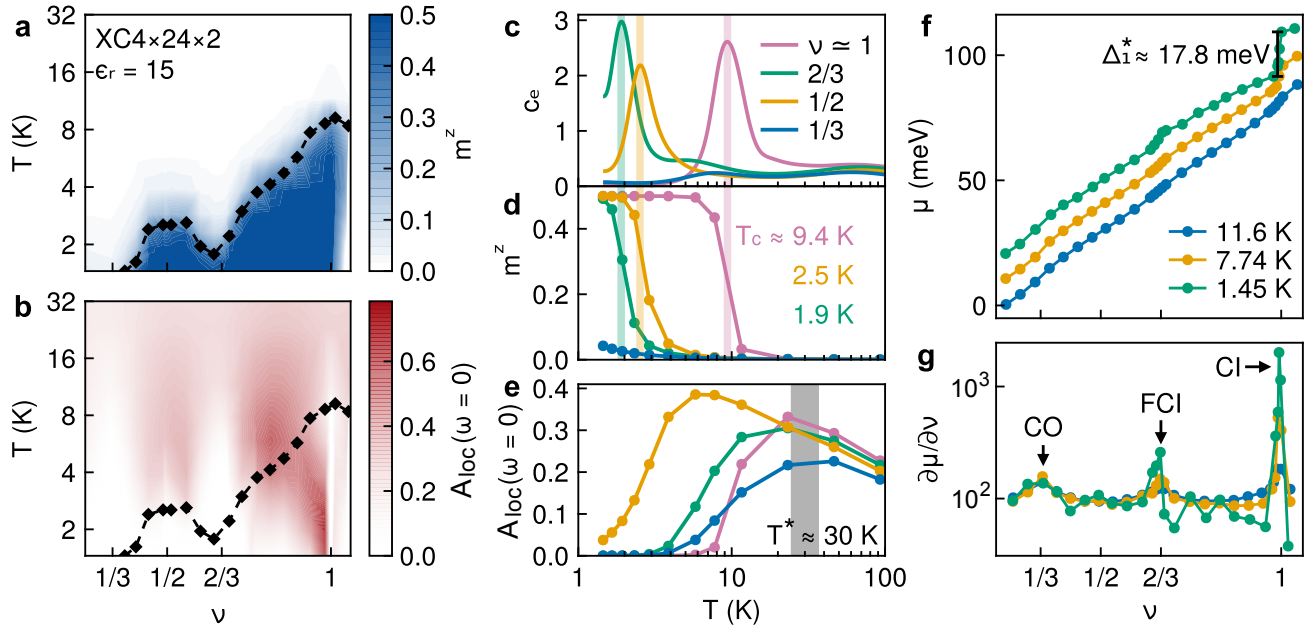


FIG. 6. Finite-temperature properties for various fillings. **a** The magnetic moment m^z and **b** the local density of states $A_{\text{loc}}(\omega = 0)$ are displayed using contour plots. The black dashed line with diamonds shows the specific heat peaks at different fillings, which indicate the FM transition. Temperature evolution of **c** specific heat c_e , **d** magnet moment m^z , and **e** $A_{\text{loc}}(\omega = 0)$ at typical fillings. **f** Chemical potential μ and **g** inverse compressibility $\kappa^{-1} = \partial\mu/\partial\nu$ for various fillings ν . The calculations are performed on a $\text{XC4} \times 24 \times 2$ and $\epsilon_r = 15$.

For general fillings, we present a contour plot of m^z in Fig. 6a. This plot reveals the FM phase transition with a Curie temperature $T_c \gtrsim 2$ K for $0.4 \lesssim \nu \lesssim 1.05$, which closely aligns with the experimental observation that FM order can be observed at 1.6 K for $0.4 \lesssim \nu \lesssim 1.2$ [8]. In Fig. 6a, the FM transition temperatures exhibit an overall decreasing trend as ν deviates from 1, except at $\nu = 2/3$, where a dip is observed. This non-monotonic behavior is also qualitatively consistent with recent experimental findings [8].

Besides the FM transition temperature, there are two additional temperature/energy scales that we can compare with experiments. As presented in the μ - ν relation in Fig. 6f, a charge gap $\Delta_1^* \approx 17.8$ meV can be estimated for $\nu = 1$ based on the low-temperature calculations. This value is in good agreement with the experimental value of 14 ± 1 meV [12], as well as to the single-particle gap $\Delta_1 \approx 18.2$ meV estimated from our spectral function results in Fig. 5. The appearance of such a charge gap leads to incompressible states and results in peaks in the inverse compressibility, $\kappa^{-1} = \partial\mu/\partial\nu$. In Fig. 6g, we estimate κ^{-1} from the μ - ν relation and find the incompressible states at $\nu = 1, 2/3$, and $1/3$ indicated by the pronounced peaks, which correspond to the ground states of CI, FCI, and CO states. Remarkably, these incompressible states have indeed been experimentally observed also by recognizing the peaks in κ^{-1} [7].

The thermal activation of charge excitation constitutes a different temperature scale that can be compared to experiments. As the temperature increases from zero in an insulating state, there are thermally activated charge excitations,

which give rise to increased longitudinal conductivity and the system behaves like a “metal”. We compute the local density of states at Fermi level, a quantity sensitively reflecting metallicity, via an imaginary-time proxy [39, 57, 58], i.e., $A_{\text{loc}}(\omega = 0) \approx \frac{2\beta}{N} \sum_{i,\sigma} \langle c_{i\sigma}^\dagger(\beta/2) c_{i\sigma} \rangle$, where N is the number of unit cells, and β is the inverse temperature. To suppress boundary effects, we average over the bulk half of the system when computing $A_{\text{loc}}(\omega = 0)$.

In Fig. 6e, we find $A_{\text{loc}}(\omega = 0)$ initially increases and then drops with increasing temperature, exhibiting a maximum about $T^* \approx 30$ K for $\nu = 1, 2/3$ and $1/3$. We refer to this as the (characteristic) thermal activation temperature, which are found consistent with the experimental activation gaps of 32 ± 2 K ($\nu = 1$), 23 ± 7 K ($\nu = 2/3$), and 15 ± 3 K ($\nu = 3/5$) observed in longitudinal resistance measurements [9]. Notably, the characteristic temperature T^* are significantly smaller than the zero-temperature charge gap, by almost an order of magnitude, which has also been experimentally observed [9, 12]. Here, our simulation accurately reproduces this phenomenon through precision many-body calculations on a realistic lattice model, suggesting that its origin may lie in strong correlation effects. Moreover, both energy scales, Δ_1 and T^* , are in turn significantly greater than the FM transition temperature, T_c , implying that it is the FM transition temperature that restricts the observation of FCI and CI phases in experiments.

In Fig. 6b, we show a contour plot of $A_{\text{loc}}(\omega = 0)$ as a function of filling and temperature. At low temperatures, $A_{\text{loc}}(\omega = 0)$ is significantly suppressed for $\nu = 1, 2/3$, and

$1/3$, aligning with the insulating bulk states of the CI, FCI, and CO at these fillings, as demonstrated by DMRG calculations. A similar suppression is observed at $\nu = 1/2$, albeit at a lower temperature, possibly since the parameter $\epsilon_r = 15$ is near the boundary between the charge-gapped QAHC and CO phases [see Fig. 4a]. On the other hand, in the small hole-doped regime to the left of $\nu = 1$ line, $A_{\text{loc}}(\omega = 0)$ clearly shows finite values till low temperature, which indicates the presence of metallic behaviors.

VI. DISCUSSION

In this study, we establish a unified theoretical framework to elucidate the intricate interplay between strong correlations and topology in tMoTe₂. Our tensor-network calculations based on a realistic model successfully explain the existence of FCI states and account for related experimental observations, while also predicting the presence of QAHC states. Unlike approaches such as ED and hybrid real-space/momentum-space DMRG [59], which rely on approximate projections onto a limited number of active bands (often just one), our framework directly incorporates multiple bands and band-mixing effects. Furthermore, our studies address a wide range of experimental observations, bridging the gap in understanding both quantum dynamics and finite-temperature effects. Specifically, we obtain the spectral functions of exotic correlated topological phases and explain the experimental finite-temperature phase diagram.

Our high-precision results not only closely align with experimental data but also provide valuable insights to future studies. Through a detailed exploration, we identify the FM_{*z*} order in the range $0.2 \lesssim \nu \leq 1$, which covers the experimentally discovered CI state at $\nu = 1$, and FCI states at fillings $\nu = 2/3, 3/5, 4/7, 4/9$, and $5/9$ in tMoTe₂ [7–13]. Our ground-state calculations unveil a rich ϵ_r - ν phase diagram featuring CI, FCI, QAHC, and CO states. For instance, at $\nu = 1/3$ we observe a robust FCI phase for $15.5 < \epsilon_r \leq 23$ and a GWC phase for $10 < \epsilon_r \leq 15.5$, where the latter agrees with recent experimental results [7]. Notably, the ϵ_r -driven quantum phase transitions between FCI and QAHC or CO phases — particularly their orders and universality classes — have yet to be clarified and warrants future investigation. The QAHC states with integer Hall conductivity $\sigma_{xy} = 1$ at fractional fillings $\nu = 1/2, 2/3, 3/5$, and $4/5$ also constitute a prediction remaining to be further explored.

Our results underscore the crucial role of well-formed density structures in stabilizing the QAHC states. In experiments, the QAHC states have been identified in graphene-based systems with higher sample quality [60–64]. Recent experiments on tMoTe₂ have revealed substantial real-space disorder through direct magnetic imaging [12], which suggests to find QAHCs in tMoTe₂ with high sample quality. Moreover, we conjecture that some of the experimentally observed FCI states at fillings such as $\nu = 1/2, 2/3$, and $3/5$ may originate from the “melting” of QAHC states, when the crystal structure is disrupted. Thermal fluctuations may also drive a transition from QAHC to FCI states [61]. Thus the determination of full

finite-temperature phase diagram of model [1] can clarify the topological Hall states in tMoTe₂ and guide experiments.

The influence of external fields on QAHCs also requires further study. QAHCs can be tuned into FCI states via applied current [61], perpendicular electric fields (displacement fields) [61–64], and other experimental parameters. In particular, the displacement field, which introduces an onsite potential difference u_D between the two sublattices, is a commonly used tunable parameter in experiments and can drive a quantum phase transition from topological Hall states to trivial insulators in tMoTe₂ [7–10]. Thus, the effects of the displacement field on various states, including the CI at $\nu = 1$, FCI at $\nu = 2/3$ [65], and QAHC at $\nu = 1/2$, remain to be explored. The insights gained from real-space models (Eqs. [1, 2, 3]) may offer valuable guidance also for studying other moiré systems with similar honeycomb superlattices [32, 66], such as twisted WSe₂, AB-stacked MoTe₂/WSe₂, and AA-stacked bilayer graphene, etc. Furthermore, a broader range of experimentally tunable parameters [32] — such as twist angle, filling, dielectric constant, and screening length — also remain to be investigated using the real-space approach introduced in the present study.

Beyond the ground-state property, our many-body results reveal three characteristic energy scales for topological Hall states: the FM transition temperature (T_c), charge activation temperature (T^*), and the zero-temperature charge gap (Δ_ν). For instance, at $\nu = 1$, we find these energy scales to be approximately $T_c \approx 9.4$ K, $T^* \approx 30$ K, and $\Delta_1 \approx 211.2$ K (18.2 meV), which closely match experimental values of about 14 K [8], 32 ± 2 K [9], and 162.5 ± 11.6 K (14 ± 1 meV) [12]. This comparison reconciles experimental contradictions, where the observed charge gaps at low temperature have been found to be more than 5 times greater than the thermal activation temperatures [9, 12]. Dynamical simulations can offer valuable insights into the observed differences between the scales. One possible explanation involves excitons as in-gap bound states. Their proliferation at finite temperature could induce strong fluctuations and renormalization effects, lowering the thermal activation threshold for excitations. Similar phenomena have been observed numerically in the topological Mott insulator phase of twisted bilayer graphene [55, 67]. Further investigation into the collective excitations in the topological Hall states — such as excitons [32], rotons, possible graviton modes [68] and fractional excitations [69] — and their comparison with spectroscopic measurements are left for future studies. Lastly, our method facilitates the exploration of exotic non-Abelian fractional excitations, particularly in the recently discovered fractional quantum spin Hall state [70].

Note added.— In preparation of our manuscript, we note a new experimental work [71] that observed a compressible metallic region between $\nu = 2/3$ to 1 that breaks spin and valley symmetry, and integer quantum anomalous Hall crystal near $\nu = 2/3$ and $3/5$ fillings. These experimental observations are consistent with our numerical results here.

ACKNOWLEDGMENTS

J.L.C., Q.Y.L., and W.L. are indebted to Bin-Bin Chen for stimulating discussions. The iDMRG calculation is based on TeNPy [48]. The dynamical and finite-temperature calculations are based on TensorKit.jl [72] and FiniteMPS.jl [73]. This work was supported by the National Natural Science Foundation of China (Grant Nos. 12222412, 12047503), National Key Projects for Research and Development of China

with Grant No. 2024YFA1409200, Innovation Program for Quantum Science and Technology (Nos. 2021ZD0301900), CAS Project for Young Scientists in Basic Research (Grant No. YSBR-057), and the Postdoctoral Fellowship Program of CPSF (Grant No. GZB20240772). We thank the HPC-ITP for the technical support and generous allocation of CPU time. X.Y.W. acknowledges financial support from the National High Magnetic Field Laboratory through National Science Foundation (NSF) Grant No. DMR-2128556, and the State of Florida.

-
- [1] N. Regnault and B. A. Bernevig, Fractional Chern insulator, *Phys. Rev. X* **1**, 021014 (2011).
 - [2] T. Neupert, L. Santos, C. Chamon, and C. Mudry, Fractional quantum Hall states at zero magnetic field, *Phys. Rev. Lett.* **106**, 236804 (2011).
 - [3] E. Tang, J.-W. Mei, and X.-G. Wen, High-temperature fractional quantum Hall states, *Phys. Rev. Lett.* **106**, 236802 (2011).
 - [4] D. Sheng, Z.-C. Gu, K. Sun, and L. Sheng, Fractional quantum Hall effect in the absence of Landau levels, *Nat. Commun.* **2**, 10.1038/ncomms1380 (2011).
 - [5] K. Sun, Z. Gu, H. Katsura, and S. Das Sarma, Nearly flatbands with nontrivial topology, *Phys. Rev. Lett.* **106**, 236803 (2011).
 - [6] F. Wu, T. Lovorn, E. Tutuc, I. Martin, and A. H. MacDonald, Topological insulators in twisted transition metal dichalcogenide homobilayers, *Phys. Rev. Lett.* **122**, 086402 (2019).
 - [7] Y. Zeng, Z. Xia, K. Kang, J. Zhu, P. Knüppel, C. Vaswani, K. Watanabe, T. Taniguchi, K. F. Mak, and J. Shan, Thermodynamic evidence of fractional Chern insulator in moiré MoTe₂, *Nature* **622**, 69 (2023).
 - [8] J. Cai, E. Anderson, C. Wang, X. Zhang, X. Liu, W. Holtzmann, Y. Zhang, F. Fan, T. Taniguchi, K. Watanabe, Y. Ran, T. Cao, L. Fu, D. Xiao, W. Yao, and X. Xu, Signatures of fractional quantum anomalous Hall states in twisted MoTe₂, *Nature* **622**, 63 (2023).
 - [9] F. Xu, Z. Sun, T. Jia, C. Liu, C. Xu, C. Li, Y. Gu, K. Watanabe, T. Taniguchi, B. Tong, J. Jia, Z. Shi, S. Jiang, Y. Zhang, X. Liu, and T. Li, Observation of integer and fractional quantum anomalous Hall effects in twisted bilayer MoTe₂, *Phys. Rev. X* **13**, 031037 (2023).
 - [10] H. Park, J. Cai, E. Anderson, Y. Zhang, J. Zhu, X. Liu, C. Wang, W. Holtzmann, C. Hu, Z. Liu, T. Taniguchi, K. Watanabe, J.-H. Chu, T. Cao, L. Fu, W. Yao, C.-Z. Chang, D. Cobden, D. Xiao, and X. Xu, Observation of fractionally quantized anomalous Hall effect, *Nature* **622**, 74 (2023).
 - [11] E. Anderson, J. Cai, A. P. Reddy, H. Park, W. Holtzmann, K. Davis, T. Taniguchi, K. Watanabe, T. Smolenski, A. İmamoğlu, T. Cao, D. Xiao, L. Fu, W. Yao, and X. Xu, Trion sensing of a zero-field composite Fermi liquid, *Nature* **635**, 590 (2024).
 - [12] E. Redekop, C. Zhang, H. Park, J. Cai, E. Anderson, O. Sheekey, T. Arp, G. Babikyan, S. Salters, K. Watanabe, T. Taniguchi, M. E. Huber, X. Xu, and A. F. Young, Direct magnetic imaging of fractional Chern insulators in twisted MoTe₂, *Nature* **635**, 584 (2024).
 - [13] Z. Ji, H. Park, M. E. Barber, C. Hu, K. Watanabe, T. Taniguchi, J.-H. Chu, X. Xu, and Z.-X. Shen, Local probe of bulk and edge states in a fractional Chern insulator, *Nature* **635**, 578 (2024).
 - [14] H. Li, U. Kumar, K. Sun, and S.-Z. Lin, Spontaneous fractional Chern insulators in transition metal dichalcogenide moiré superlattices, *Phys. Rev. Res.* **3**, L032070 (2021).
 - [15] Y. H. Kwan, G. Wagner, J. Yu, A. K. Dagnino, Y. Jiang, X. Xu, B. A. Bernevig, T. Neupert, and N. Regnault, When could Abelian fractional topological insulators exist in twisted MoTe₂ (and other systems) (2024), arXiv:2407.02560 [cond-mat.str-el].
 - [16] V. Crépel and L. Fu, Anomalous Hall metal and fractional Chern insulator in twisted transition metal dichalcogenides, *Phys. Rev. B* **107**, L201109 (2023).
 - [17] A. P. Reddy and L. Fu, Toward a global phase diagram of the fractional quantum anomalous Hall effect, *Phys. Rev. B* **108**, 245159 (2023).
 - [18] C. Wang, X.-W. Zhang, X. Liu, Y. He, X. Xu, Y. Ran, T. Cao, and D. Xiao, Fractional Chern insulator in twisted bilayer MoTe₂, *Phys. Rev. Lett.* **132**, 036501 (2024).
 - [19] A. P. Reddy, F. Alsallom, Y. Zhang, T. Devakul, and L. Fu, Fractional quantum anomalous Hall states in twisted bilayer MoTe₂ and WSe₂, *Phys. Rev. B* **108**, 085117 (2023).
 - [20] A. Abouelkomsan, A. P. Reddy, L. Fu, and E. J. Bergholtz, Band mixing in the quantum anomalous Hall regime of twisted semiconductor bilayers, *Phys. Rev. B* **109**, L121107 (2024).
 - [21] X. Shen, C. Wang, R. Guo, Z. Xu, W. Duan, and Y. Xu, Stabilizing fractional Chern insulators via exchange interaction in moiré systems (2024), arXiv:2405.12294 [cond-mat.str-el].
 - [22] T. Zakkala, D. Luo, and L. Fu, Structure factor and topological bound of twisted bilayer semiconductors at fractional fillings (2024), arXiv:2411.03496 [cond-mat.str-el].
 - [23] C. Xu, J. Li, Y. Xu, Z. Bi, and Y. Zhang, Maximally localized wannier functions, interaction models, and fractional quantum anomalous Hall effect in twisted bilayer MoTe₂, *Proc. Natl. Acad. Sci. U.S.A.* **121**, e2316749121 (2024).
 - [24] D. N. Sheng, A. P. Reddy, A. Abouelkomsan, E. J. Bergholtz, and L. Fu, Quantum anomalous Hall crystal at fractional filling of moiré superlattices, *Phys. Rev. Lett.* **133**, 066601 (2024).
 - [25] H. Goldman, A. P. Reddy, N. Paul, and L. Fu, Zero-field composite Fermi liquid in twisted semiconductor bilayers, *Phys. Rev. Lett.* **131**, 136501 (2023).
 - [26] J. Dong, J. Wang, P. J. Ledwith, A. Vishwanath, and D. E. Parker, Composite Fermi liquid at zero magnetic field in twisted MoTe₂, *Phys. Rev. Lett.* **131**, 136502 (2023).
 - [27] M. Wang, X. Wang, and O. Vafek, Phase diagram of twisted bilayer MoTe₂ in a magnetic field with an account for the electron-electron interaction, *Phys. Rev. B* **110**, L201107 (2024).
 - [28] T. Wang, T. Devakul, M. P. Zaletel, and L. Fu, Topological magnets and magnons in twisted bilayer MoTe₂ and WSe₂ (2023), arXiv:2306.02501 [cond-mat.str-el].

- [29] X. Liu, Y. He, C. Wang, X.-W. Zhang, T. Cao, and D. Xiao, Gate-tunable antiferromagnetic Chern insulator in twisted bilayer transition metal dichalcogenides, *Phys. Rev. Lett.* **132**, 146401 (2024).
- [30] W.-X. Qiu, B. Li, X.-J. Luo, and F. Wu, Interaction-driven topological phase diagram of twisted bilayer MoTe₂, *Phys. Rev. X* **13**, 041026 (2023).
- [31] J. Yu, J. Herzog-Arbeitman, M. Wang, O. Vafek, B. A. Bernevig, and N. Regnault, Fractional Chern insulators versus nonmagnetic states in twisted bilayer MoTe₂, *Phys. Rev. B* **109**, 045147 (2024).
- [32] K. F. Mak and J. Shan, Semiconductor moiré materials, *Nat. Nanotechnol.* **17**, 686 (2022).
- [33] Y. Wang, J. Choe, E. Anderson, W. Li, J. Ingham, E. A. Arsenault, Y. Li, X. Hu, T. Taniguchi, K. Watanabe, X. Roy, D. Basov, D. Xiao, R. Queiroz, J. C. Hone, X. Xu, and X. Y. Zhu, Hidden states and dynamics of fractional fillings in tMoTe₂ moiré superlattices (2025), arXiv:2502.21153 [cond-mat.str-el].
- [34] H. Li, S. Li, E. C. Regan, D. Wang, W. Zhao, S. Kahn, K. Yumigeta, M. Blei, T. Taniguchi, K. Watanabe, S. Tongay, A. Zettl, M. F. Crommie, and F. Wang, Imaging two-dimensional generalized Wigner crystals, *Nature* **597**, 650 (2021).
- [35] T. Devakul, The new quantum anomalous Hall effects require new concepts, *J. Club Condens. Matter Phys.* **10.36471/JCCM_August_2024.01** (2024).
- [36] S. R. White, Density matrix formulation for quantum renormalization groups, *Phys. Rev. Lett.* **69**, 2863 (1992).
- [37] I. P. McCulloch, Infinite size density matrix renormalization group, revisited (2008), arXiv:0804.2509 [cond-mat.str-el].
- [38] U. Schollwöck, The density-matrix renormalization group in the age of matrix product states, *Annals of Physics* **326**, 96 (2011), january 2011 Special Issue.
- [39] Q. Li, Y. Gao, Y.-Y. He, Y. Qi, B.-B. Chen, and W. Li, Tangent space approach for thermal tensor network simulations of the 2D Hubbard model, *Phys. Rev. Lett.* **130**, 226502 (2023).
- [40] D.-W. Qu, Q. Li, S.-S. Gong, Y. Qi, W. Li, and G. Su, Phase diagram, *d*-wave superconductivity, and pseudogap of the $t - t' - J$ model at finite temperature, *Phys. Rev. Lett.* **133**, 256003 (2024).
- [41] J. Haegeman, J. I. Cirac, T. J. Osborne, I. Pižorn, H. Verschelde, and F. Verstraete, Time-Dependent Variational Principle for Quantum Lattices, *Phys. Rev. Lett.* **107**, 070601 (2011).
- [42] J. Haegeman, C. Lubich, I. Oseledets, B. Vandereycken, and F. Verstraete, Unifying time evolution and optimization with matrix product states, *Phys. Rev. B* **94**, 165116 (2016).
- [43] T. Wang, M. Wang, W. Kim, S. G. Louie, L. Fu, and M. P. Zaletel, Topology, magnetism and charge order in twisted MoTe₂ at higher integer hole fillings (2023), arXiv:2312.12531 [cond-mat.str-el].
- [44] Y. Jia, J. Yu, J. Liu, J. Herzog-Arbeitman, Z. Qi, H. Pi, N. Regnault, H. Weng, B. A. Bernevig, and Q. Wu, Moiré fractional Chern insulators. i. first-principles calculations and continuum models of twisted bilayer MoTe₂, *Phys. Rev. B* **109**, 205121 (2024).
- [45] D. Xiao, G.-B. Liu, W. Feng, X. Xu, and W. Yao, Coupled spin and valley physics in monolayers of MoS₂ and other group-VI dichalcogenides, *Phys. Rev. Lett.* **108**, 196802 (2012).
- [46] Supplementary Material section I present details of the model construction. Section II presents various ground-state results including magnetic gaps for various fillings, ground-state phase diagram for $\nu = 1$, charge pumping results for fractional fillings $\nu = 3/5, 4/5, 3/7, 4/7, 5/7, 6/7, 4/9, 5/9$, and charge density distributions at $\nu = 3/5, 4/5$. Section III provides complementary datasets for finite-temperature calculations. Section IV details the computational methodology for determining the zero-temperature spectral function and presents convergence check. Ref. [74–81] is included in the Supplementary Material.
- [47] A. A. Soluyanov and D. Vanderbilt, Wannier representation of F_2 topological insulators, *Phys. Rev. B* **83**, 035108 (2011).
- [48] J. Hauschild, J. Unfried, S. Anand, B. Andrews, M. Bintz, U. Borla, S. Divic, M. Drescher, J. Geiger, M. Hefel, K. Hémery, W. Kadow, J. Kemp, N. Kirchner, V. S. Liu, G. Möller, D. Parker, M. Rader, A. Romen, S. Scalet, L. Schoonderwoerd, M. Schulz, T. Soejima, P. Thoma, Y. Wu, P. Zechmann, L. Zweng, R. S. K. Mong, M. P. Zaletel, and F. Pollmann, Tensor network Python (TeNPy) version 1, *SciPost Phys. Codebases* **41** (2024).
- [49] T. D. Kühner and S. R. White, Dynamical correlation functions using the density matrix renormalization group, *Phys. Rev. B* **60**, 335 (1999).
- [50] Q. Li, J. Cui, and W. Li, Detecting confined and deconfined spinons in dynamical quantum simulations, *Phys. Rev. Research* **4**, 013193 (2022).
- [51] A. Gleis, J.-W. Li, and J. von Delft, Controlled bond expansion for density matrix renormalization group ground state search at single-site costs, *Physical Review Letters* **130**, 246402 (2023).
- [52] J.-W. Li, A. Gleis, and J. von Delft, Time-dependent variational principle with controlled bond expansion for matrix product states, *Phys. Rev. Lett.* **133**, 026401 (2024).
- [53] R. B. Laughlin, Quantized Hall conductivity in two dimensions, *Phys. Rev. B* **23**, 5632 (1981).
- [54] A. G. Grushin, J. Motruk, M. P. Zaletel, and F. Pollmann, Characterization and stability of a fermionic $\nu = 1/3$ fractional Chern insulator, *Phys. Rev. B* **91**, 035136 (2015).
- [55] B.-B. Chen, Y. D. Liao, Z. Chen, O. Vafek, J. Kang, W. Li, and Z. Y. Meng, Realization of topological Mott insulator in a twisted bilayer graphene lattice model, *Nat. Commun.* **12**, 5480 (2021).
- [56] S. M. Girvin, A. H. MacDonald, and P. M. Platzman, Magneto-roton theory of collective excitations in the fractional quantum Hall effect, *Phys. Rev. B* **33**, 2481 (1986).
- [57] W. Jiang, Y. Liu, A. Klein, Y. Wang, K. Sun, A. V. Chubukov, and Z. Y. Meng, Monte Carlo study of the pseudogap and superconductivity emerging from quantum magnetic fluctuations, *Nat. Commun.* **13**, 2655 (2022).
- [58] S. Lederer, Y. Schattner, E. Berg, and S. A. Kivelson, Superconductivity and non-Fermi liquid behavior near a nematic quantum critical point, *Proc. Natl. Acad. Sci. U.S.A.* **114**, 4905 (2017).
- [59] T. Soejima, D. E. Parker, N. Bultinck, J. Hauschild, and M. P. Zaletel, Efficient simulation of moiré materials using the density matrix renormalization group, *Phys. Rev. B* **102**, 205111 (2020).
- [60] R. Su, D. Waters, B. Zhou, K. Watanabe, T. Taniguchi, Y.-H. Zhang, M. Yankowitz, and J. Folk, Moiré-driven topological electronic crystals in twisted graphene, *Nature* **637**, 1084 (2025).
- [61] Z. Lu, T. Han, Y. Yao, Z. Hadjri, J. Yang, J. Seo, L. Shi, S. Ye, K. Watanabe, T. Taniguchi, and L. Ju, Extended quantum anomalous Hall states in graphene/hBN moiré superlattices, *Nature* **637**, 1090 (2025).
- [62] S. H. Aronson, T. Han, Z. Lu, Y. Yao, K. Watanabe, T. Taniguchi, L. Ju, and R. C. Ashoori, Displacement field-controlled fractional Chern insulators and charge density waves in a graphene/hBN moiré superlattice (2024), arXiv:2408.11220 [cond-mat.mes-hall].

- [63] D. Waters, A. Okounkova, R. Su, B. Zhou, J. Yao, K. Watanabe, T. Taniguchi, X. Xu, Y.-H. Zhang, J. Folk, and M. Yankowitz, Chern insulators at integer and fractional filling in moiré pentalayer graphene, *Phys. Rev. X* **15**, 011045 (2025).
- [64] Z. Zhang, J. Yang, B. Xie, Z. Feng, S. Zhang, K. Watanabe, T. Taniguchi, X. Yang, Q. Dai, T. Liu, D. Liu, K. Liu, Z. Song, J. Liu, and X. Lu, Commensurate and incommensurate Chern insulators in magic-angle bilayer graphene (2024), [arXiv:2408.12509 \[cond-mat.mes-hall\]](https://arxiv.org/abs/2408.12509).
- [65] P. Sharma, Y. Peng, and D. N. Sheng, Topological quantum phase transitions driven by a displacement field in twisted MoTe₂ bilayers, *Phys. Rev. B* **110**, 125142 (2024).
- [66] E. Y. Andrei and A. H. MacDonald, Graphene bilayers with a twist, *Nat. Mater.* **19**, 1265 (2020).
- [67] X. Lin, B.-B. Chen, W. Li, Z. Y. Meng, and T. Shi, Exciton proliferation and fate of the topological mott insulator in a twisted bilayer graphene lattice model, *Phys. Rev. Lett.* **128**, 157201 (2022).
- [68] J. Liang, Z. Liu, Z. Yang, Y. Huang, U. Wurstbauer, C. R. Dean, K. W. West, L. N. Pfeiffer, L. Du, and A. Pinczuk, Evidence for chiral graviton modes in fractional quantum Hall liquids, *Nature* **628**, 78 (2024).
- [69] Direct observation of anyonic braiding statistics, *Nat. Phys.* **16**, 931 (2020).
- [70] K. Kang, B. Shen, Y. Qiu, Y. Zeng, Z. Xia, K. Watanabe, T. Taniguchi, J. Shan, and K. F. Mak, Evidence of the fractional quantum spin Hall effect in moiré MoTe₂, *Nature* **628**, 522 (2024).
- [71] F. Xu, Z. Sun, J. Li, C. Zheng, C. Xu, J. Gao, T. Jia, K. Watanabe, T. Taniguchi, B. Tong, L. Lu, J. Jia, Z. Shi, S. Jiang, Y. Zhang, Y. Zhang, S. Lei, X. Liu, and T. Li, Signatures of unconventional superconductivity near reentrant and fractional quantum anomalous hall insulators (2025), [arXiv:2504.06972 \[cond-mat.mes-hall\]](https://arxiv.org/abs/2504.06972).
- [72] J. Haegeman, <https://github.com/Jutho/TensorKit.jl>.
- [73] Q. Li, <https://github.com/Qiaoyi-Li/FiniteMPS.jl>.
- [74] T. Lu and L. H. Santos, Fractional Chern insulators in twisted bilayer MoTe₂: A composite fermion perspective, *Phys. Rev. Lett.* **133**, 186602 (2024).
- [75] H. C. Po, H. Watanabe, and A. Vishwanath, Fragile topology and Wannier obstructions, *Phys. Rev. Lett.* **121**, 126402 (2018).
- [76] L. Zou, H. C. Po, A. Vishwanath, and T. Senthil, Band structure of twisted bilayer graphene: Emergent symmetries, commensurate approximants, and Wannier obstructions, *Phys. Rev. B* **98**, 085435 (2018).
- [77] H. C. Po, L. Zou, A. Vishwanath, and T. Senthil, Origin of mott insulating behavior and superconductivity in twisted bilayer graphene, *Phys. Rev. X* **8**, 031089 (2018).
- [78] X. Wang and O. Vafek, Diagnosis of explicit symmetry breaking in the tight-binding constructions for symmetry-protected topological systems, *Phys. Rev. B* **102**, 075142 (2020).
- [79] F. Guinea and N. R. Walet, Electrostatic effects, band distortions, and superconductivity in twisted graphene bilayers, *Proc. Natl. Acad. Sci. U.S.A.* **115**, 13174 (2018).
- [80] O. Vafek and J. Kang, Lattice model for the Coulomb interacting chiral limit of magic-angle twisted bilayer graphene: Symmetries, obstructions, and excitations, *Phys. Rev. B* **104**, 075143 (2021).
- [81] F. D. M. Haldane, Model for a quantum Hall effect without Landau levels: Condensed-matter realization of the "parity anomaly", *Phys. Rev. Lett.* **61**, 2015 (1988).

Supplementary Materials for

Fractional Chern Insulator and Quantum Anomalous Hall Crystal in Twisted MoTe₂

Chen *et al.*

I. MODEL HAMILTONIAN

Here we present a derivation of the model Hamiltonian of tMoTe₂ from the continuum electronic model. The experimentally relevant twist angle for this work is in the range of 3.4° ~ 3.9°, where fractionalized quantum anomalous Hall effect has been observed [7–13].

A. Continuum model of twisted bilayer MoTe₂

Monolayer MoTe₂ features strong spin-orbit coupling [45], such that the spin (\uparrow, \downarrow) and valley (\mathbf{K}, \mathbf{K}') quantum numbers are locked. We hereby use the convention of $\{\mathbf{K}, \uparrow\}$ and $\{\mathbf{K}', \downarrow\}$ to label the electronic states.

Focusing on $\{\mathbf{K}, \uparrow\}$, the relevant low energy degrees of freedom are the valence bands of the two MoTe₂ layers. The moiré superlattice potential hybridizes the two layers, with a minimal model given by the following continuum Hamiltonian [6]:

$$H_{\uparrow} = \int d^2\mathbf{r} \begin{pmatrix} \psi_{b\uparrow}^\dagger(\mathbf{r}) & \psi_{t\uparrow}^\dagger(\mathbf{r}) \end{pmatrix} \begin{pmatrix} h_b(\mathbf{p}) + \Delta_b(\mathbf{r}) + \frac{u_D}{2} & \Delta_T(\mathbf{r}) \\ \Delta_T^*(\mathbf{r}) & h_t(\mathbf{p}) + \Delta_t(\mathbf{r}) - \frac{u_D}{2} \end{pmatrix} \begin{pmatrix} \psi_{b\uparrow}(\mathbf{r}) \\ \psi_{t\uparrow}(\mathbf{r}) \end{pmatrix}. \quad (\text{S1})$$

Here $\psi_{l\uparrow}^\dagger(\mathbf{r})$ creates an electron in layer $l = b, t$, with spin \uparrow and in valley \mathbf{K} , and at position \mathbf{r} . For convenience we drop the valley subscript and label the electrons by their spin quantum number. $h_l(\mathbf{p}) = -(\mathbf{p} - \hbar\mathbf{K}_l)^2/2m^*$ is kinetic energy, with $\mathbf{p} = -i\hbar\nabla_{\mathbf{r}}$ and effective mass m^* . \mathbf{K}_l points sit at the corners of the hexagonal moiré Brillouin zone (see Fig. S1(a) inset). We describe the effect of displacement field \mathbf{D} by adding a potential difference u_D between two layers. $\Delta_{b(t)}(\mathbf{r}) = 2V \sum_{j=1,3,5} \cos(\mathbf{G}_j \cdot \mathbf{r} \pm \phi)$ is the intralayer potential for bottom (top) layer, and $\Delta_T(\mathbf{r}) = w(1 + e^{-i\mathbf{G}_2 \cdot \mathbf{r}} + e^{-i\mathbf{G}_3 \cdot \mathbf{r}})$ is interlayer tunneling potential. $\mathbf{G}_{i=1,\dots,6}$ are the six smallest reciprocal lattice vectors, with $\mathbf{G}_1 = \frac{4\pi}{\sqrt{3}L_M} \hat{x}$ along the $+x$ direction, and \mathbf{G}_{i+1} is the vector obtained by rotating \mathbf{G}_i 60° counterclockwise. Here $L_M \approx a_0/\theta$ is the moiré unit vector length, with θ the twist angle and a_0 the MoTe₂ lattice spacing.

	a_0 [\AA]	m^* [m_e]	V [meV]	ϕ	ω [meV]
Ref. [6]	3.47	0.62	8.0	-89.6°	-8.5
Ref. [43]	3.55	0.62	17.0	107.7°	-16.0
Ref. [18]	3.52	0.6	20.8	107.7°	-23.8
Ref. [19]	3.52	0.62	7.5	-100°	-11.3

TABLE II. Continuum model parameters from literature.

The continuum model parameters are obtained by fitting the continuum model dispersion to DFT calculations [6, 18, 19, 43, 44], with different sets of parameters obtained depending on the literature (see Table II). Besides, Ref. [44] has included terms beyond those included in Eq. (S1). For concreteness, we utilize the parameters specified in Ref. [43] and a twist angle of $\theta = 3.89^\circ$. Although our tensor-network results are expected to be qualitatively consistent with other model parameters, a likely exception is Ref.[19], as it predicts a different sequence of moiré band Chern numbers compared to the other DFT calculations. Figure S1(a) shows the energy dispersions in valley \mathbf{K} and spin \uparrow in the moiré Brillouin zone. Energy dispersions in valley \mathbf{K}' and spin \downarrow are related by time reversal symmetry. Experimentally, FCI states are achieved by doping holes into the valence bands, corresponding to partial fillings of the band colored in red.

B. Tight binding fit to the continuum model

With the exception of Ref. [19], other DFT calculations predict the upper two moiré bands of a given valley carry Chern numbers +1 and -1 respectively, including the one we used for this work. This allows us to construct exponentially localized

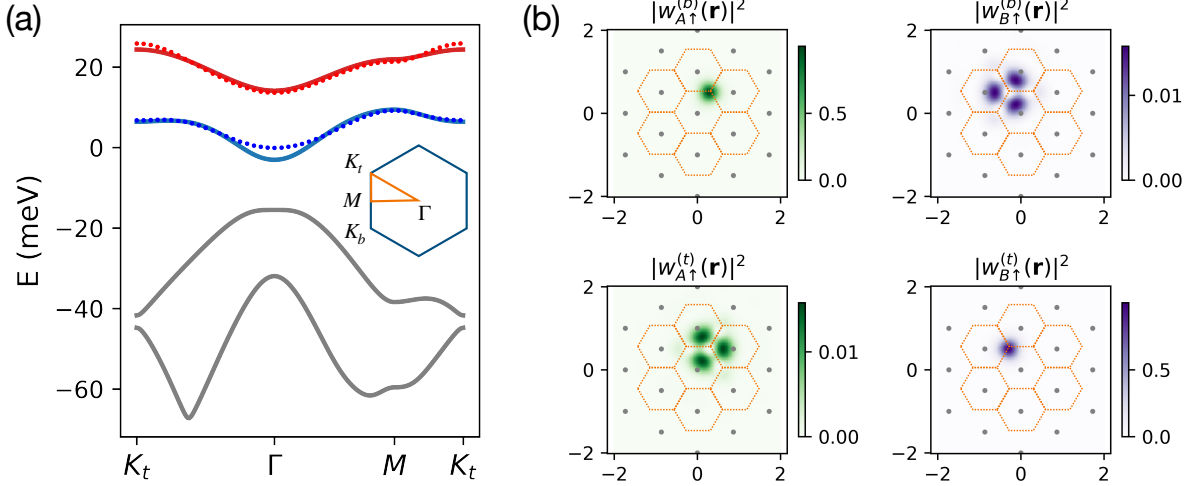


FIG. S1. (a) Solid lines: electronic dispersions of valley **K** and spin \uparrow in the moiré Brillouin zone. The two colored bands (blue and red), along with their time reversed partners in valley **K'** and spin \downarrow , are the most relevant low energy bands for experiments. The inset depicts the moiré Brillouin zone and the linecut (orange) along which the dispersion is drawn. Dotted lines: tight-binding fits to the dispersions of the upper two bands. (b) Real space electronic density profile of the pair of exponentially localized Wannier orbitals, normalized with respect to the peak density. The real space coordinates are measured with the length of the moiré unit cell vector set to 1. The Wannier orbitals reside mostly at the honeycomb lattice sites, corresponding to the XM/MX stacking regions of the tMoTe₂. The pair of Wannier orbitals, labeled by *A* and *B* respectively, are also predominantly layer resolved. Specifically, $\psi_{A\uparrow}$ reside predominantly on the bottom layer (upper left panel), whereas $\psi_{B\uparrow}$ resides predominantly on the top layer (lower right panel).

Wannier orbitals without suffering from topological obstruction of a band composite with a finite Chern number [47]. Using the trial state procedure discussed in Ref. [47], we construct exponentially localized Wannier orbitals to describe the Hilbert space spanned by the upper two valence bands per valley, see Fig. S1(b). The two Wannier orbitals per valley reside predominantly on the honeycomb lattice, which is the dual lattice of the moiré triangular lattice made of AA stackings. We hereby label these states as $w_A(\mathbf{r})$ and $w_B(\mathbf{r})$ respectively, with the subscripts *A*, *B* denoting the center of the Wannier orbitals. Separately, these two orbitals are layer polarized, with $w_{A(B)}(\mathbf{r})$ having most orbital weights on the bottom (top) layer.

In summary, the two Chern bands per valley can be represented using the Wannier orbital basis states, $\{w_{i,\sigma}(\mathbf{r})\}$, where $\sigma = \uparrow, \downarrow$. *i* denotes the Wannier orbital center at $\mathbf{R} + \tau$, where $\tau = A, B$ is the position of a sublattice inside a moiré unit cell centered at $\mathbf{R} = m\mathbf{L}_1 + n\mathbf{L}_2$. $\mathbf{L}_{i=1,2}$ are moiré unit cell vectors. Note that the Wannier orbital is a spinor in the layer basis.

The tight-binding model is therefore given as:

$$H_{\text{TB}} = \sum_{ij,\sigma} t_{ij,\sigma} c_{i\sigma}^\dagger c_{j\sigma} - \sum_{i,\sigma} \mu_{i\sigma} c_{i\sigma}^\dagger c_{i\sigma}, \quad (\text{S2})$$

where $c_{i\sigma}^\dagger$ creates an electron in the Wannier orbital labeled by *i* and spin σ . Due to time reversal symmetry $t_{ij,\downarrow} = t_{ij,\uparrow}^*$. The hopping amplitudes $t_{ij,\uparrow}$ and the onsite terms μ_i are shown in Fig. S2(a).

In this work, we truncate the hopping terms to the third nearest neighbor, corresponding to the black dashed circle in Fig. S2(a). The tight-binding dispersion is plotted as dotted line in Fig. S1(a), showing its comparison with the continuum model.

C. Screened Coulomb interaction

We consider a dual-gate screened Coulomb interaction given by

$$H_U = \frac{1}{2A} \iint d^2\mathbf{r} d^2\mathbf{r}' V(\mathbf{r} - \mathbf{r}') \hat{P}\rho(\mathbf{r}) \hat{P} \hat{P}\rho(\mathbf{r}') \hat{P}, \quad (\text{S3})$$

where A is the area of the system. The interaction coefficient and its Fourier transform are given by

$$V(\mathbf{r} - \mathbf{r}') = \frac{e^2}{4\pi\epsilon_0\epsilon_r|\mathbf{r} - \mathbf{r}'|} e^{-|\mathbf{r} - \mathbf{r}'|/\xi},$$

$$V_{\mathbf{q}} = \frac{1}{A} \frac{e^2}{2\epsilon_0\epsilon_r} \frac{\tanh(|\mathbf{q}|\xi)}{|\mathbf{q}|},$$

where ϵ_0 is the vacuum permittivity, ϵ_r is the relative dielectric constant, ξ is the screening length. $\rho(\mathbf{r})$ is the electron density operator:

$$\rho(\mathbf{r}) = \sum_{l,\sigma} \psi_{l,\sigma}^\dagger(\mathbf{r}) \psi_{l,\sigma}(\mathbf{r}).$$

\hat{P} is the projector onto the narrow bands of interest, i.e., the colored bands in Fig. S1(a). In the Wannier orbital basis, the projected density operator becomes:

$$\hat{P}\rho(\mathbf{r})\hat{P} = \sum_{ij,\sigma} \left[w_{i,\sigma}^\dagger(\mathbf{r}) w_{j,\sigma}(\mathbf{r}) \right] c_{i\sigma}^\dagger c_{j\sigma}.$$

Finally, the Coulomb interaction projected onto the low energy Hilbert space is given as:

$$H_U = \frac{1}{2} \sum_{ijkl,\sigma\sigma'} V_{ijkl}^{\sigma,\sigma'} c_{i\sigma}^\dagger c_{j\sigma} c_{k\sigma'}^\dagger c_{l\sigma'}, \quad (\text{S4})$$

where

$$V_{ijkl}^{\sigma,\sigma'} = \frac{1}{A} \iint d^2\mathbf{r} d^2\mathbf{r}' V(\mathbf{r} - \mathbf{r}') \left[w_{i,\sigma}^\dagger(\mathbf{r}) w_{j,\sigma}(\mathbf{r}) \right] \left[w_{k,\sigma'}^\dagger(\mathbf{r}') w_{l,\sigma'}(\mathbf{r}') \right].$$

Evaluating above integration directly in real space can be challenging. In practice, we switch to Fourier space and calculate the following:

$$V_{ijkl}^{\sigma,\sigma'} = \sum_{\mathbf{q}} V_{\mathbf{q}} \left[\int d^2\mathbf{r} w_{i,\sigma}^\dagger(\mathbf{r}) e^{-i\mathbf{q}\cdot\mathbf{r}} w_{j,\sigma}(\mathbf{r}) \right] \left[\int d^2\mathbf{r}' w_{k,\sigma'}^\dagger(\mathbf{r}') e^{i\mathbf{q}\cdot\mathbf{r}'} w_{l,\sigma'}(\mathbf{r}') \right].$$

The two bracketed integrals can be evaluated conveniently by representing Wannier orbitals using the Bloch basis states.

Given the exponential localization of the Wannier orbitals, interaction coefficients with $i \neq j$ or $k \neq l$ (assisted hopping terms) are small compared to density-density interactions with $i = j$ and $k = l$. For relative dielectric constant $\epsilon_r = 10$ and screening distance $\xi \approx 5.77L_m \simeq 30$ nm, interaction coefficients with $i \neq j$ or $k \neq l$ are all ≤ 1 meV. We hereby drop these terms in our simulations, and approximate the projected Coulomb interaction by density-density interactions,

$$H_U \approx \frac{1}{2} \sum_{ij,\sigma\sigma'} V_{ii,jj}^{\sigma,\sigma'} n_{i\sigma} n_{j\sigma'} \equiv U \sum_{i\sigma} n_{i\uparrow} n_{i\downarrow} + \sum_{i < j, \sigma\sigma'} V_{ij} n_{i\sigma} n_{j\sigma'}. \quad (\text{S5})$$

Fig. S2(b) shows the interaction coefficients $\{U, V_{ij}\}$. Due to the exponential localization of the Wannier orbitals, to a good degree of quantitative accuracy, we find the following approximate expression for the density density interactions:

$$U \approx \frac{1192.71}{\epsilon_r} \text{meV},$$

$$V(\mathbf{r}) \approx \frac{276.92}{\epsilon_r} \frac{L_m}{|\mathbf{r}|} \exp\left(-\frac{|\mathbf{r}|/L_m}{\xi/L_m}\right) \text{meV},$$

where L_m is the length of the moiré unit cell vector. This analytic expression is used in the tensor-network simulations. Furthermore, due to system size constraints, we cut off the interaction terms beyond the dotted circles shown in Fig. S2(b). In the main text, we choose a shorter screening length of $\xi = 2L_m$, which results in an even smaller truncation error for the long-range couplings.

We note a key distinction here for tMoTe₂ as compared to the twisted bilayer graphene (TBG): due to the nontrivial topology in TBG, it is not possible to construct exponentially localized and symmetric Wannier orbitals [47, 75–78], and the Coulomb interaction projected onto the narrow bands can have additional contributions beyond the density-density interaction in Eq. (S5), notably the assisted hopping terms [55, 79, 80]. However, for tMoTe₂ the Wannier orbitals are sufficiently localized on the honeycomb lattice sites (see Fig. S1b), and as a result, the interaction is effectively of the Coulomb density-density form [23].

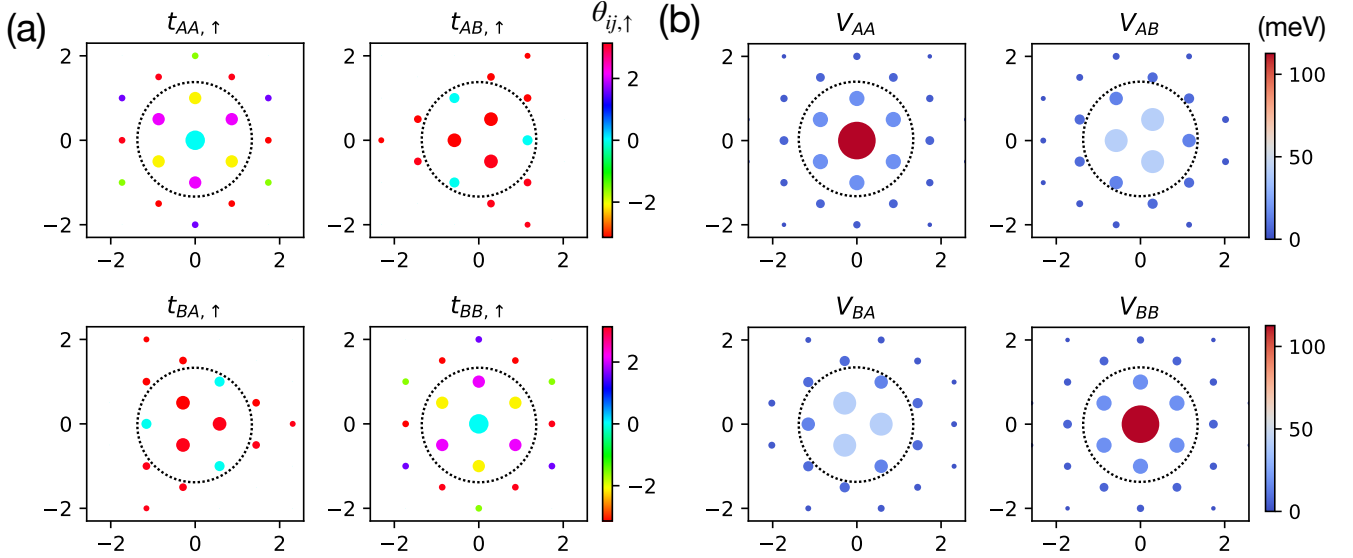


FIG. S2. (a) Hopping amplitudes $t_{ij,\sigma}$ in real space, where the length of the moiré unit cell vector is set to 1. Here we use the area size of the dots to denote the magnitude and the color to denote the phase (in unit of radian), such that $t_{ij,\sigma} \equiv |t_{ij,\sigma}| e^{i\theta_{ij,\sigma}}$. The onsite terms $\mu_{A,B}$ are depicted as cyan dots at $(0,0)$ in the upper left and lower right panels. In tensor-network simulations we kept hopping terms enclosed by the black dashed circles. (b) Projected density-density interactions. The strength of the interactions are denoted by both dot size and color. The interaction strengths are obtained for screening distance $\xi = 30$ nm and relative dielectric constant $\epsilon_r = 10$. In tensor-network simulations we keep interaction terms enclosed by the black dashed circles (and with a shorter screening length ξ).

D. Particle-hole transformation

The parameters in Eq. (S1) are assumed to lead to experimentally measured band dispersions at the reference state $|\Omega\rangle$ corresponding to hole filling 0, i.e., when the chemical potential is placed above the moiré bands depicted in Fig. S1(a). However, with respect to $|\Omega\rangle$, the projected Coulomb interaction in Eq. (S4) will renormalize the band dispersions away from that obtained using Eq. (S1). This leads to double counting, and a quadratic order counter term needs to be added to avert this effect.

Alternatively, we can perform a particle-hole transformation $d_{i\sigma}^\dagger = c_{i\sigma}$ which inverts the non-interacting band structure (as well as the hopping parameters and chemical potential), while simultaneously we preserve the same functional form for the projected density density interactions but with $n_{i\sigma} = d_{i\sigma}^\dagger d_{i\sigma}$. Such a transformation has been used in previous theoretical studies on tMoTe₂ (see, e.g., Ref. [19]). Here $|\Omega\rangle$ will be a vacuum state for d fermions, and therefore the density-density interaction will *not* lead to band renormalizations.

Therefore, instead of stating our results for hole fillings $-1 \leq \nu_h < 0$, we report results for electron fillings $0 < \nu \leq 1$. Accordingly, we present the band structure of the model described by Eq. (S2) in Fig. S3, which includes hopping terms up to the third nearest neighbors following the particle-hole transformation. Without interactions, electrons only fill the lower band [see, Fig. S3(c)] when filling factor $\nu \leq 1$.

II. SUPPLEMENTARY GROUND-STATE RESULTS

A. Magnetic gaps for various fillings

Figure S4 displays the relative energy $E(S_z) - E(\text{FM}_z)$ per iDMRG unit cell, with respect to the fully polarized FM_z sector (maximum $|S_z|$). Our findings reveal a finite gap above the FM_z ground state for $\nu \gtrsim 0.2$, suggesting that the FM_z order remains stable except for filling fractions ν very close to zero. Moreover, we simulate the model with $10 \leq \epsilon_r \leq 20$, with the results summarized in the magnetic phase diagram Fig. 1d in the main article.

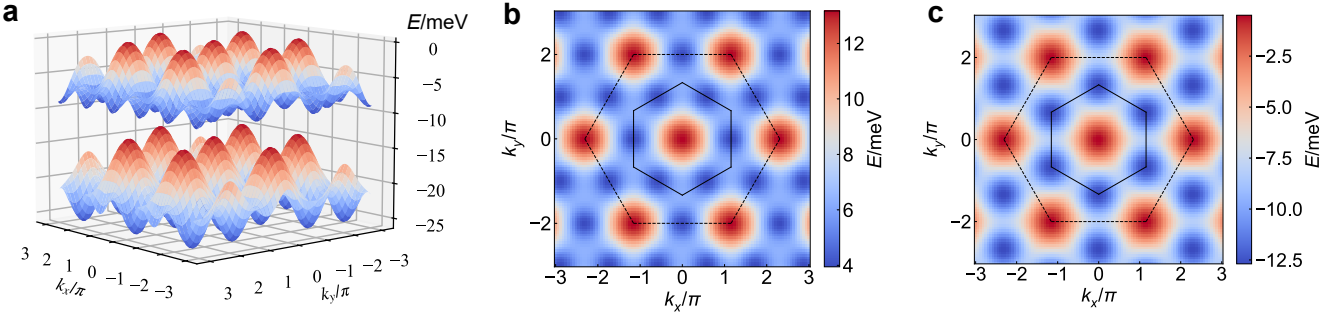


FIG. S3. **a** Band structure of the tight-binding model (S2) with hopping terms up to the third nearest neighbor after particle-hole transformation. Panels **b** and **c** represent the upper and lower bands, respectively. The smaller (larger) honeycomb with black solid (dashed) line represents the first (enlarged) Brillouin zone.

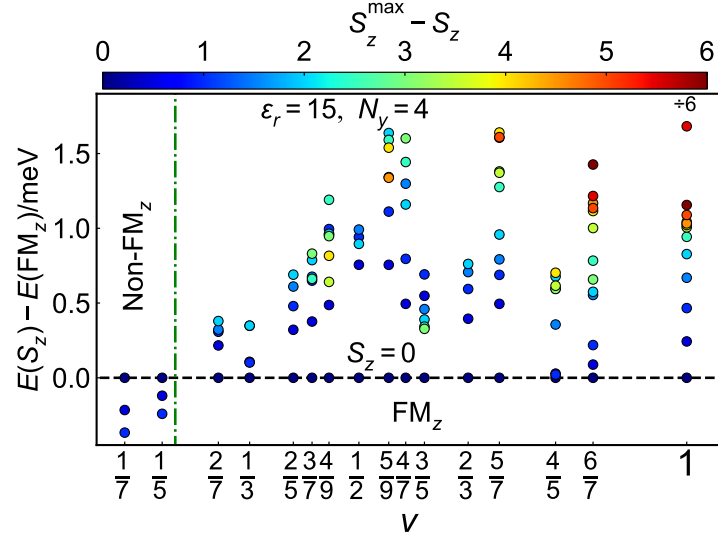


FIG. S4. Energy levels in different spin sectors and various fillings. The dielectric constant is fixed as $\epsilon_r = 15$. $E(S_z)$ are shown relative to the FM_z state, and the results indicate that the FM_z state is energetically favorable for $\nu \gtrsim 0.2$.

B. Ground-state results for $\nu = 1$

We present results of the model Eq. (1) in the main text at an integer filling factor of $\nu = 1$. By analyzing the ground-state energies across various spin- S_z sectors, we consistently find that the ground states are always in the FM_z ordered phase for dielectric constants $\epsilon_r \in [10, 20]$, and for system sizes $N_y = 4, 5, 6$. Meanwhile, as shown in Fig. S5a, the maximum $\rho(\mathbf{q}) \simeq 0$ in the whole range, indicating a uniform state.

In the absence of interactions, the model Eq. (1) can be viewed as a generalization of the renowned Haldane model [81], which possesses a CI state with Chern number $|\mathcal{C}| = 1$ and quantum Hall conductivity $\sigma_{xy} = 1$. With interactions switched on, we simulate the Hall conductivity through charge pumping, as demonstrated in Fig. S5b for several ϵ_r and $N_y = 4, 5, 6$, with DMRG calculations. Our results reveal that the insertion of a single quantum flux ($\Phi_y = 2\pi$) leads to a charge pumping of $|\Delta Q| = 1$, confirming that the ground state is indeed a CI state with a quantized Hall conductivity $\sigma_{xy} = \frac{2\pi|\Delta Q|}{\Phi_y} = 1$, even with the strong coupling U and $V(r)$.

As shown in Fig. S5a, through a scan of the parameter space, we identify a robust CI phase at least within the range $10 \leq \epsilon_r \leq 20$, indicating that the CI phase is highly stable against interactions and potentially persists over a wide range of dielectric constants. Nonetheless, in general cases the incorporation of interaction terms U and $V(r)$ can profoundly enrich the electronic states, thereby requiring precision many-body calculations to determine their properties.

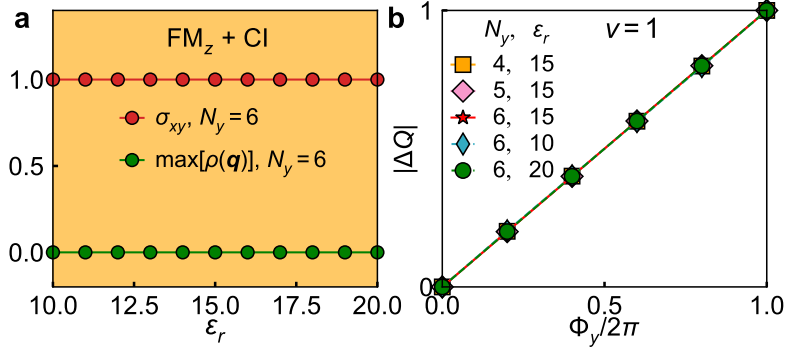


FIG. S5. Uniform Chern insulator at $\nu = 1$ filling. **a** Phase diagram containing only the CI state tuned by ϵ_r , showcasing the maximum of $\rho(\mathbf{q})$ and Hall conductivity σ_{xy} . **b** Charge pumping results $|\Delta Q|$ for various N_y and ϵ_r parameters, measured after inserting a flux $\Phi_y = 2\pi$. The inset provides a schematic illustration of the charge pumping simulation process.

C. Ground-state results for fillings $\nu = p/q$ with $q \geq 5$

Besides the fillings $\nu = p/q$ with small denominators $q = 1, 2, 3$ discussed in the main text, we have also simulated larger values of $q = 5, 7, 9$.

1. Charge pumping results

As shown in Fig. S6, we present results of charge pumping simulations for various fractional fillings $\nu = p/q = 3/5, 4/5, 3/7, 4/7, 5/7, 6/7, 4/9$, and $5/9$. As the denominator q increases, the required XC length N_x (which is typically several integer multiples of q) also increases, while the charge gap for potential FCIs may decrease. The simulations are more challenging and time-consuming, as smaller evolution step sizes and many more steps are needed to ensure adiabaticity. In practice, we limit N_y to a maximum of 5 in our simulations and present results satisfying the adiabatic evolution condition. Further studies involving

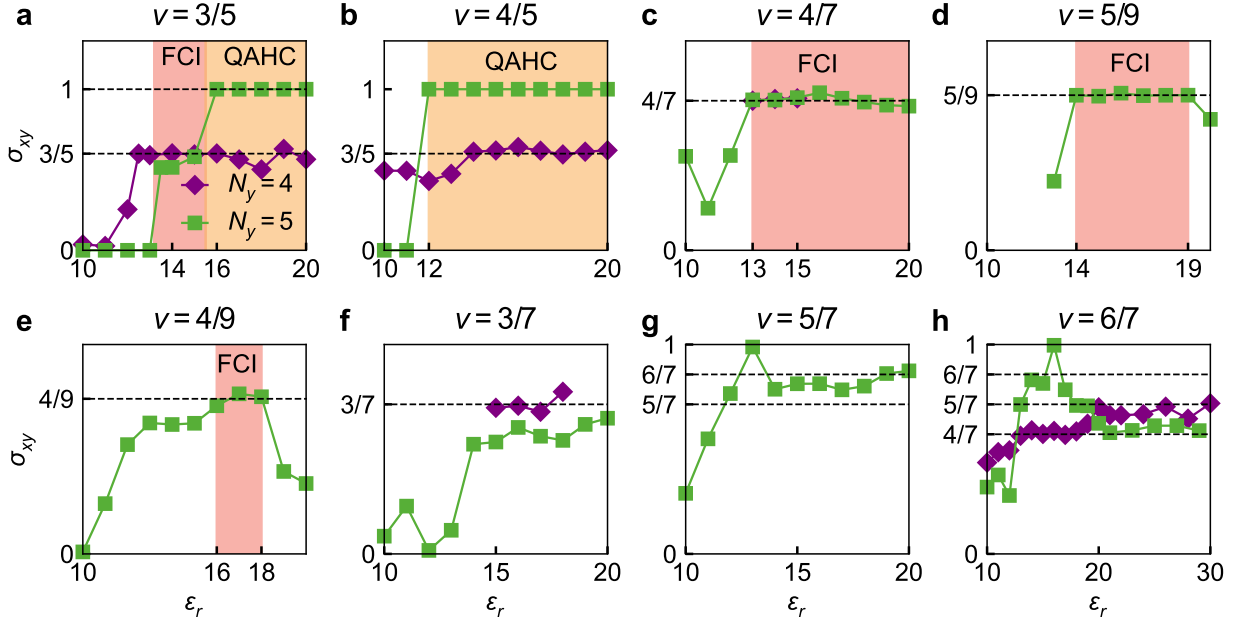


FIG. S6. Panels **a-h** show charge pumping results with varying ϵ_r for $\nu = 3/5, 4/5, 4/7, 5/9, 4/9, 3/7, 5/7$, and $6/7$, respectively. The presence of FCI and QAHC states on $N_y = 5$ cylinders are marked with red and orange, respectively. It is FM_z for all these parameters. In all panels, the purple diamonds represent $N_y = 4$ data, and the green squares represent the $N_y = 5$ results.

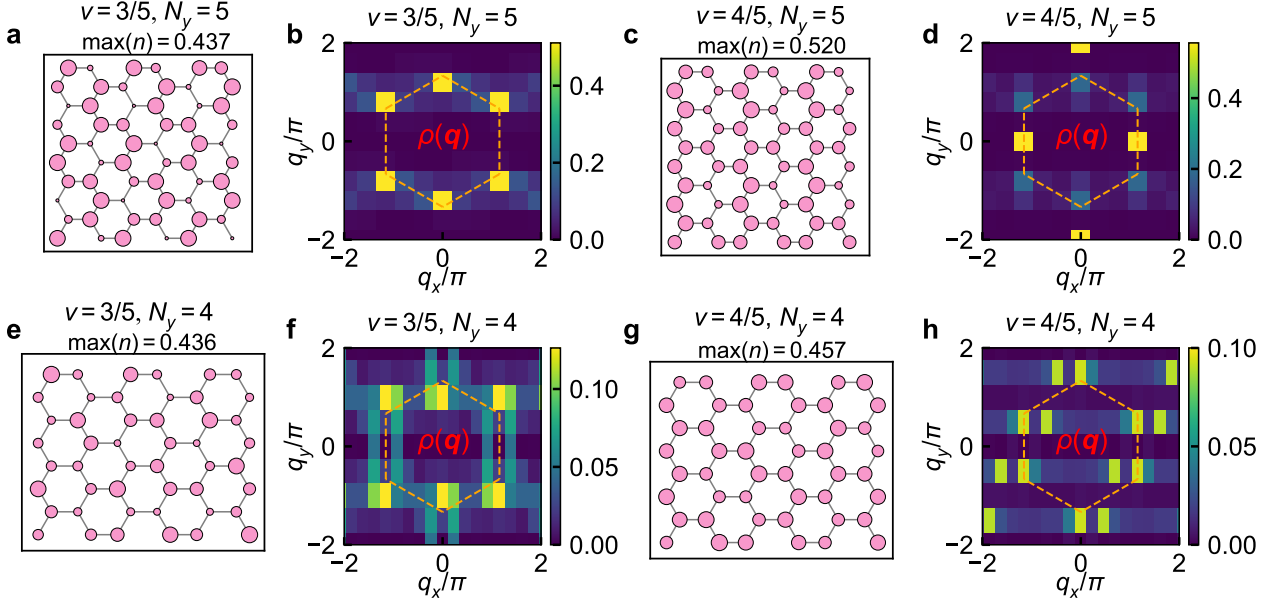


FIG. S7. DMRG results of **a** $n(r)$ and **b** $\rho(\mathbf{q})$ for QAHC with filling $\nu = 3/5$ (with $\epsilon_r = 15$ and on $N_y = 5$ cylinder). Panels **(e,f)** show same quantities as panels **(a,b)** but for FCI states on $N_y = 4$. Panels **(c,d,g,h)** show results for filling $\nu = 4/5$ on $N_y = 4, 5$ cylinders, with $\epsilon_r = 18$. The orange hexagon with dashed lines represent the first Brillouin zones of the honeycomb lattice.

wider cylinders are necessary to validate our findings and better approach the thermodynamic limit.

Figures S6c and d highlight robust FCIs within a wide range, $13 \lesssim \epsilon_r \lesssim 20$ and $14 \lesssim \epsilon_r \lesssim 19$, for $\nu = 4/7$ and $5/9$, respectively. Panels a and e depict weaker FCIs with a narrower range ($\Delta\epsilon_r \sim 2$) for $\nu = 3/5$ and $4/9$. For the case of $\nu = 3/5$, a QAHC phase is observed for $16 \lesssim \epsilon_r \lesssim 20$ on the $N_y = 5$ cylinder. Distinctly, FCI states with $\sigma_{xy} \simeq \nu = 3/5$ emerges for $N_y = 4$ cylinder. This difference is possibly due to geometric constraints, as discussed in the main text for the $\nu = 1/2, 2/3$ cases. A similar phenomenon is observed for $\nu = 4/5$ in Fig. S6b, with a subtle difference that $\sigma_{xy} = 3/5 \neq \nu$ for the FCI.

For the case of $\nu = 6/7$, we can observe results such as $\sigma_{xy} = 4/7 \neq \nu$ in Fig. S6h. However, the relevant range of ϵ_r varies significantly with N_y , which suggests that further verification through simulations on larger system sizes is required. For the cases of $\nu = 3/7$ and $\nu = 5/7$, although the Hall conductivity σ_{xy} is found to be nonzero, the values are not (fractionally) quantized, indicating the absence of clear FCIs in Figs. S6f and g.

For FCI states where $\sigma_{xy} < \nu$, such as for $\nu = 4/5$ (and possibly also for $\nu = 6/7$), we conjecture that this Hall conductivity might be attributed to the partial carriers involved in the formation of FCIs, while the remaining carriers form an insulating non-uniform charge distribution. As shown in $\rho(\mathbf{q})$ in Fig. S7h, these states exhibit peaks rather than vanished values, which is different from the typical FCI at $\nu = 1/3$ in Fig. 2g. Moreover, such states could also be classified as "fractal FCIs," arising from the full filling of fractal bands in the composite fermion picture [74].

2. Density distribution for $\nu = 3/5$ and $4/5$

In Fig. S7, we present the charge distribution $n(r)$ in real space and $\rho(\mathbf{q})$ in momentum space for $\nu = 3/5$ and $\nu = 4/5$ fillings. For $N_y = 5$, the charge distribution exhibits a well-defined CO structure for both fillings, which is consistent with the QAHC phase with Hall conductivity $\sigma_{xy} = 1$, as previously discussed. However, for $N_y = 4$, such a CO structure is incompatible with the limited width and thus disrupted, with its strength (i.e., the maximum of $\rho(\mathbf{q})$) becoming much weaker, and instead, a FCI state emerges, highlighting the sensitivity of the system to lattice geometry and the interplay between CO and topological orders.

3. Phase diagram

Above results for various fillings $\nu = p/q$ with $q \geq 5$ are summarized in the phase diagram S8. We observe robust FCIs for $\nu = 4/7$ (with $13 \leq \epsilon_r \leq 20$) and $\nu = 5/9$ ($14 \leq \epsilon_r \leq 19$), spanning a wide range of ϵ_r . Additionally, FCIs with a narrower

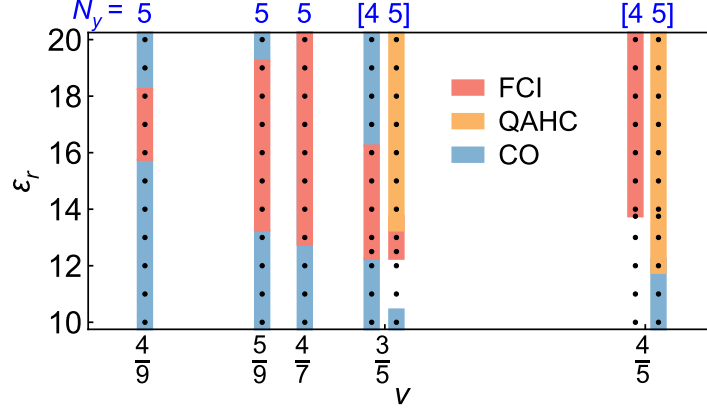


FIG. S8. The phase diagram with various fillings $\nu = p/q$ for $q \geq 5$. Solid dots without color bar represent topologically trivial states with uniform density distributions. The lattice widths used, $N_y = 4$ and 5 , are indicated. For fillings $\nu = 3/5$ and $4/5$, both widths are considered. Across the entire phase diagram, FM_z order is checked to be present.

ϵ_r range ($\Delta\epsilon_r \sim 2$) are observed for $\nu = 4/9$ and $3/5$. For $\nu = 3/5$ and $4/5$ fillings, QAHC states are found for $N_y = 5$. On the other hand, FCI states with $\sigma_{xy} = 3/5$ (for both $\nu = 3/5$ and $4/5$ fillings) are found for $N_y = 4$ (see Figs. S6 and S7 for details). The sensitivity of FCI or QAHC phase to the cylinder width is similar to that observed in the $\nu = 1/2$ case discussed in the main text. Except for the topological states for $\nu = 4/5$ filling that are not yet seen in experiments, the FCIs at $\nu = 3/5$, $4/7$, $4/9$, and $5/9$ obtained in our simulations are consistent with recent experiments.

III. SUPPLEMENTARY FINITE-TEMPERATURE RESULTS

In Fig. S9, we present additional finite-temperature benchmark results to validate the model simplification in the main text. It involves the reduction from local Hilbert space dimension $d = 4$ in the Hubbard-type model Eq. (1) to $d = 3$ in the spinful t - V model Eq. (2). The double-occupancy states of the spinful t - V model are projected out. Since the case with filling $\nu = 1$ may potentially have the largest double occupancy D_n , we select $\nu = 1$ as a stringent test case.

Figure S9(a) shows the electron density distribution $n_\sigma(x) = \frac{1}{N_y} \sum_{i=1}^{N_y} \langle n_{i\sigma} \rangle$, where i runs over the N_y sites sharing the same x -coordinates. Due to the open boundary along the x -direction, short-range oscillations appear. Thus, we use only the central 1/4 to 3/4 of the sites as bulk sites for averaging. This method is applied throughout the text below unless otherwise specified.

We calculate the average double occupancy $D_n = \frac{1}{N_{\text{bulk}}} \sum_{i \in \text{bulk}} \langle n_{i\uparrow} n_{i\downarrow} \rangle$ of the original model Eq. (1) with local dimension $d = 4$. As shown in Fig. S9(b), D_n gets suppressed at about $T_d^* \approx 662$ K and almost diminishes as the temperature drops below about 100 K. Therefore, we conclude that the projected local Hilbert space dimension $d = 3$ in Eq. (2) does not affect the low-temperature behavior of the original model Eq. (1).

We also examine the impacts of the Zeeman pinning field. As depicted in Fig. S9(c, d), higher pinning fields h^z marginally sharpen the FM phase transition but only slightly modify the transition temperature T_c . Consequently, our selection of $h^z = 0.01$ in the main text is thoroughly justified.

IV. COMPUTATION METHOD AND CONVERGENCE CHECK OF THE SPECTRAL FUNCTION

Let $\alpha \in \{A, B\}$ be the index of sublattice, fermionic operators in momentum space are defined as

$$c_{\mathbf{k}\alpha} = \frac{1}{\sqrt{N_x N_y}} \sum_{i \in \alpha} e^{-i\mathbf{k} \cdot \mathbf{r}_i} c_i. \quad (\text{S6})$$

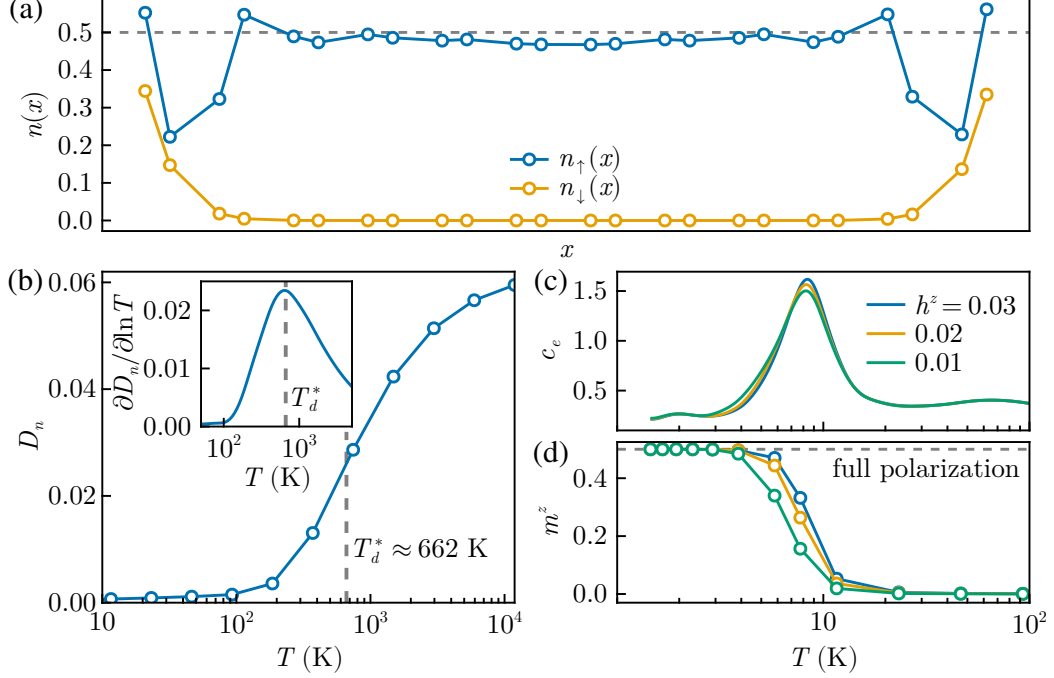


FIG. S9. Finite-temperature results for an XC4 \times 12 \times 2 with parameters $\nu = 1$ and $\epsilon_r = 15$. (a) Electron density distribution $n_{\uparrow(\downarrow)}(x)$ at $T \approx 1.45$ K. (b) Temperature evolution of the bulk-averaged double occupancy D_n . The inset shows $\partial D_n / \partial \ln T$, which determines a characteristic temperature $T_d^* \approx 662$ K where D_n is suppressed rapidly. (c,d) Comparison of low-temperature electron specific heat c_e and magnetic moment m^z per electron for different pinning fields h^z . Panels (a,b) and (c,d) are computed with bond dimension $D = 2000$ and $D = 3000$, respectively.

The sublattice-resolved retarded Green's function reads

$$\begin{aligned}
 G_{\alpha\beta}^R(\mathbf{k}, \omega) &= -i \int_0^\infty dt e^{i\omega t} \langle \text{GS} | \left\{ c_{\mathbf{k}\alpha}(t), c_{\mathbf{k}\beta}^\dagger \right\} | \text{GS} \rangle \\
 &= -i \int_0^\infty dt e^{i\omega t} \left[\langle \text{GS} | c_{\mathbf{k}\alpha}(t) c_{\mathbf{k}\beta}^\dagger | \text{GS} \rangle + \overline{\langle \text{GS} | c_{\mathbf{k}\alpha}^\dagger(t) c_{\mathbf{k}\beta} | \text{GS} \rangle} \right] \\
 &= -i \int_0^\infty dt e^{i(\omega+E_g)t} \langle \text{GS} | c_{\mathbf{k}\alpha} e^{-iHt} c_{\mathbf{k}\beta}^\dagger | \text{GS} \rangle + i \int_0^\infty dt e^{-i(\omega-E_g)t} \overline{\langle \text{GS} | c_{\mathbf{k}\alpha}^\dagger e^{-iHt} c_{\mathbf{k}\beta} | \text{GS} \rangle}
 \end{aligned} \tag{S7}$$

where $|\text{GS}\rangle$ denotes the ground state.

It remains to compute the expectation values like $\langle \text{GS} | c_{\mathbf{k}\alpha} e^{-iHt} c_{\mathbf{k}\beta}^\dagger | \text{GS} \rangle$ and $\langle \text{GS} | c_{\mathbf{k}\alpha}^\dagger e^{-iHt} c_{\mathbf{k}\beta} | \text{GS} \rangle$. Considering the former one, it can be written as the inner product of two states $e^{iHt/2} c_{\mathbf{k}\alpha}^\dagger | \text{GS} \rangle$ and $e^{-iHt/2} c_{\mathbf{k}\beta} | \text{GS} \rangle$. We first use standard DMRG algorithm to obtain the ground state $|\text{GS}\rangle$ that is represented as a MPS. Then, we act the operator $c_{\mathbf{k}\alpha}^\dagger$, which can be efficiently represented as a MPO with bond dimension $D = 2$ via automata, on the ground state MPS and obtain the new MPS $c_{\mathbf{k}\alpha}^\dagger | \text{GS} \rangle$. $c_{\mathbf{k}\beta} | \text{GS} \rangle$ is obtained similarly. Then, we use the TDVP approach (accelerated with the controlled bond expansion) to perform the backward and forward time evolution to the former and the latter, which results in the two states $e^{iHt/2} c_{\mathbf{k}\alpha}^\dagger | \text{GS} \rangle$ and $e^{-iHt/2} c_{\mathbf{k}\beta}^\dagger | \text{GS} \rangle$, respectively. The inner product is calculated after each time step and the sequence of $\langle \text{GS} | c_{\mathbf{k}\alpha} e^{-iHt} c_{\mathbf{k}\beta}^\dagger | \text{GS} \rangle$ is collected to be used in the numerical integration latter. Regarding $\langle \text{GS} | c_{\mathbf{k}\alpha} e^{-iHt} c_{\mathbf{k}\beta}^\dagger | \text{GS} \rangle$ in the second term of Eq. (S7), the procedure is similar except that the creation and annihilation operators are exchanged.

In the non-interacting case, the two bare bands are obtained by forming proper linear combinations of the fermionic operators from the two sublattices. A similar procedure can be applied in the interacting case by numerically diagonalizing the equal-time

correlation matrices, i.e.

$$\begin{bmatrix} \langle c_{\mathbf{k}A}c_{\mathbf{k}A}^\dagger \rangle & \langle c_{\mathbf{k}A}c_{\mathbf{k}B}^\dagger \rangle \\ \langle c_{\mathbf{k}B}c_{\mathbf{k}A}^\dagger \rangle & \langle c_{\mathbf{k}B}c_{\mathbf{k}B}^\dagger \rangle \end{bmatrix} = V \text{diag} \left[\langle f_{\mathbf{k}\downarrow}f_{\mathbf{k}\downarrow}^\dagger \rangle, \langle f_{\mathbf{k}\uparrow}f_{\mathbf{k}\uparrow}^\dagger \rangle \right] V^\dagger \quad (\text{S8})$$

where $f_{\mathbf{k}\downarrow}$ and $f_{\mathbf{k}\uparrow}$ is the fermionic operators belonging to the lower and upper bands, respectively, with the unitary matrix V storing the coefficients of the linear combination. Written in the new representation, we get the band-resolved Green's function via $G_{mp}^R(\mathbf{k}, \omega) = \sum_{\alpha\beta} V_{\alpha m}^* G_{\alpha\beta}^R(\mathbf{k}, \omega) V_{\beta p}$ where $m, p \in \{l, u\}$ label the bands. Finally, computing spectral function $A_{mm}(\mathbf{k}, \omega) = -2\text{Im}G_{mm}^R(\mathbf{k}, \omega)$ is straightforward after we get the retarded Green's function.

Due to the finite evolution time ($t_{\max} = 3 \text{ meV}^{-1}$ in practical calculations), the numerical integration can only be performed after being multiplied by a window function $W(t)$ with vanished value beyond t_{\max} , i.e.

$$\begin{aligned} \tilde{G}_{\alpha\beta}^R(\mathbf{k}, \omega) &\equiv -i \int_0^{t_{\max}} dt W(t) e^{i(\omega+E_g)t} \langle \text{GS} | c_{\mathbf{k}\alpha} e^{-iHt} c_{\mathbf{k}\beta}^\dagger | \text{GS} \rangle + i \int_0^{t_{\max}} dt W(t) e^{-i(\omega-E_g)t} \langle \text{GS} | c_{\mathbf{k}\alpha}^\dagger e^{-iHt} c_{\mathbf{k}\beta} | \text{GS} \rangle \\ &= \int_{-\infty}^{\infty} \frac{d\omega'}{2\pi} \widetilde{W}(\omega - \omega') G_{\alpha\beta}^R(\mathbf{k}, \omega') \equiv \frac{1}{2\pi} \widetilde{W}(\omega) * G_{\alpha\beta}^R(\mathbf{k}, \omega), \end{aligned} \quad (\text{S9})$$

where $\widetilde{W}(\omega) \equiv \int_{-\infty}^{\infty} dt e^{i\omega t} W(t)$. Therefore, the effect of a finite t_{\max} reduces to the convolution of a window function with the original Green's function. Directly performing the integration in $[0, t_{\max}]$ is equivalent to applying a rectangular window function, which leads to strongly non-physical oscillations in frequency domain. In practice, we use the Parzen window function

$$W(t) = \begin{cases} 1 - 6|t/t_{\max}|^2 + 6|t/t_{\max}|^3, & |t| \leq t_{\max}/2 \\ 2(1 - |t/t_{\max}|)^3, & t_{\max}/2 < |t| \leq t_{\max} \\ 0, & |t| > t_{\max}, \end{cases} \quad (\text{S10})$$

with $\widetilde{W}(\omega) = 192 \sin^4(\omega t_{\max}/4)/(\omega^4 t_{\max}^3)$, as shown in Fig. S10(a,b). The frequency resolution is about $8/t_{\max} \approx 2.67 \text{ meV}$, defined by the full width at half maximum (FWHM) of the convolution kernel.

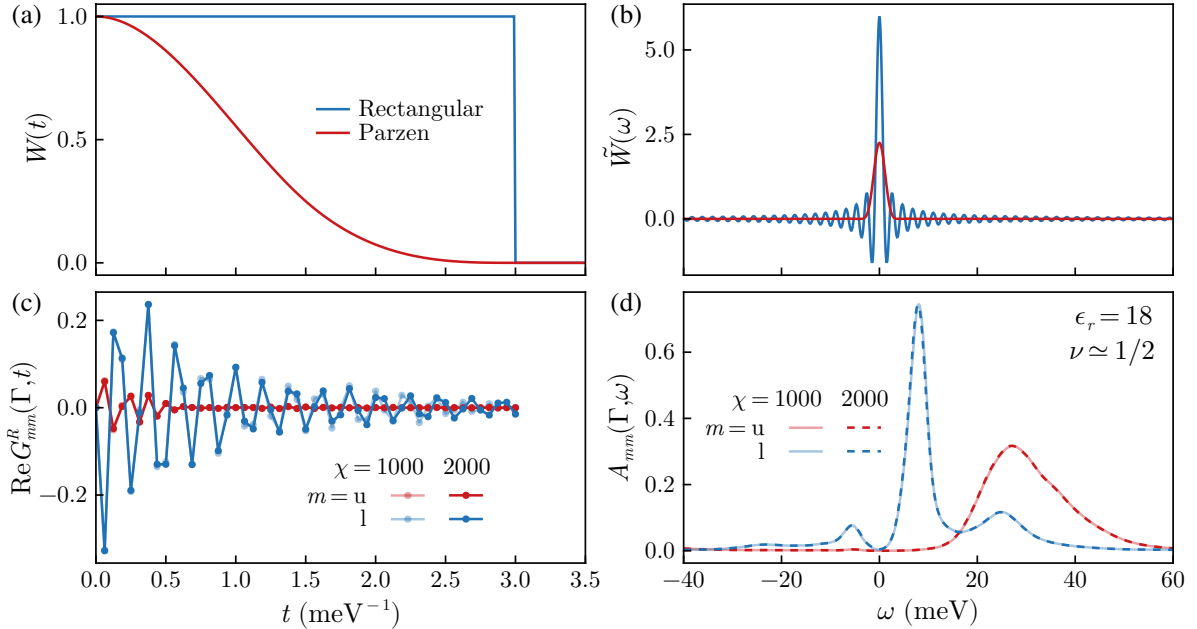


FIG. S10. (a) The rectangular window and Parzen window with $t_{\max} = 3 \text{ meV}^{-1}$, whose Fourier transformations are shown in (b). (c) Data convergence of the real part of the retarded Green's function $\text{Re}G_{mm}^R(\mathbf{k}, t)$ and (d) the corresponding spectral function $A_{mm}(\mathbf{k}, \omega)$. We show the $A_{mm}(\mathbf{k}, \omega)$ results at $\mathbf{k} = \Gamma$, evaluated in the QAHC phase with $\nu \simeq 1/2$ and $\epsilon_r = 18$. The results provide representative benchmarks, since the presented spectral function in (d) exhibits several characteristic features, including a sharp peak, satellite peaks, and excitation continua.

The single-particle spectral function data are obtained with a bond dimension $\chi = 1000$. The convergence with respect to the bond dimension for a typical QAHC case is shown in Fig. S10(c,d). Compared with a larger $\chi = 2000$, the difference in retarded Green's function $G_{mm}^R(\mathbf{k}, t)$ is very small during the time evolution, while the corresponding spectral function $A_{mm}(\mathbf{k}, \omega)$ virtually coincide. This can be understood as the deviations in $G_{mm}^R(\mathbf{k}, t)$ at relatively long time t , become suppressed by the window function.